

Multi-Field Dilaton Screening Beyond the Thin-Shell Mechanism

Philippe Brax,¹ Carsten van de Bruck,² Anne-Christine Davis,³ and Adam Smith²

¹*Institut de Physique Théorique, Université Paris-Saclay, Gif-sur-Yvette, France*

²*School of Mathematical and Physical Sciences, University of Sheffield, Sheffield, United Kingdom*

³*DAMTP & Kavli Institute of Cosmology (KICC),
Cambridge University, Cambridge, United Kingdom*

(Dated: March 17, 2026)

We analyse screening in multi-field scalar-tensor theories, focusing on systems with a dilaton coupled to matter and an axion with a dilaton-dependent kinetic term, in the presence of both planetary and stellar density profiles. Using analytic arguments and fully coupled numerical solutions, we identify a regime in which full screening for a dark-energy-light, effectively unpinned string-dilaton, can occur without fine-tuning. The backreaction of the dilaton's partnered axion field can suppress the exterior scalar charge by selecting a minimum-energy configuration (the BBQ mechanism), yielding robust screening for generic axion gradients. In this regime screening is achieved by cancelling the dilaton's gradient rather than localising it. This reduces the exterior scalar charge and allows for gravity tests in the solar system to be passed. We then show that the more familiar thin-shell intuition need not apply in the multi-field setting. Axion surface gradients can drastically reshape the dilaton profile and drive a more localised transition without generically suppressing the fifth force. The exterior charge can remain essentially unchanged or even be enhanced as the shell is made thinner by a kinetically coupled field. Multi-field two-derivative dynamics therefore decouple localisation in thin shells from screening, evade single-field no-go arguments, and reopen viable parameter space for cosmologically light dilaton-like scalars with strong couplings to matter.

I. INTRODUCTION

Modern cosmological data are now precise enough that new light degrees of freedom are no longer a purely speculative idea. Scalar fields with masses at or below the Hubble scale are being tested directly through the expansion history and the growth of structure in the Universe [1–11]. This has renewed interest in theoretically controlled scalar sectors that can modify late-time dynamics [12–14], relieve parameter-level tensions [15–20], or imprint signatures that distinguish dynamical dark energy from a cosmological constant [21–27]. In parallel, ultraviolet completions of gravity such as string theory rarely deliver a low energy effective theory containing a single isolated scalar field [28–32]. They generically contain multiple light fields, including moduli associated with couplings and scales and axions protected by approximate shift symmetries, whose leading interactions are governed as much by field-space geometry as by potentials [33]. The appearance of such scalars in gauge couplings and other fundamental parameters generically induces couplings to the myriad of fields in the Standard Model. The natural question is therefore not whether light scalars exist, but how they can remain compatible with stringent local tests while retaining cosmological relevance.

Any light scalar that couples to matter mediates a new long-range interaction. Laboratory experiments, solar-system dynamics, and astrophysical observations place extremely strong bounds on such fifth forces [34–39]. Viable scalar-tensor theories must therefore include a screening mechanism that suppresses the scalar response of dense objects, allowing the field to be active on large scales while effectively decoupling in local environments where constraints are tightest.

Among the most theoretically well-motivated light scalars, dilatons appear both as the scalar partner of the graviton in the universal closed-string sector and its low-energy effective action [40–43], and as the scalar mode exposed when Jordan-Brans-Dicke-type scalar-tensor theories are rewritten in the Einstein frame by a conformal rescaling [44, 45]; their couplings can be dynamically suppressed by the least-coupling principle and its runaway and environmentally dependent extensions [46–53]. They provide a minimal parametrisation of how effective couplings and masses can depend on a light field. Screening a dilaton with constant matter coupling is fundamentally difficult. In the standard telling of the story the dilaton develops a density-dependent effective potential and sits at different minima inside and outside dense objects. For exponential couplings the field excursion between these minima is logarithmic in the density contrast. When considering realistic astrophysical density contrasts this excursion is parametrically large, and the dilaton is forced to have non-zero spatial gradients exterior to sources to reach the asymptotic minimum and standard thin-shell screening fails [46, 50]. The fifth force remains essentially unscreened unless the coupling is tuned extremely small. This obstruction becomes especially constraining in scenarios where cosmological analyses prefer, or comfortably accommodate, matter couplings far larger than would be allowed without screening [54–57], as can occur when a light scalar affects both gravity and microphysics through controlled variations of particle masses across key epochs [46].

A central point of this paper is that the single-field assumption when drawing conclusions about matter couplings and their correspondence with observables is not generic from either an ultraviolet or an effective-field-

theory viewpoint. Once more than one light scalar is present, the kinetic sector defines a curved target-space geometry and associated two-derivative interactions cannot be removed by field redefinitions. In static configurations, gradients of one scalar can then source another even if potentials are shallow or symmetries suppress direct couplings. Screening can therefore be controlled by genuinely multi-field two-derivative dynamics that do not exist in any one-field truncation. The sign and magnitude of field-space curvature couplings can decide whether an additional field helps screening or makes it worse, independently of the detailed form of the potentials.

In this work we analyse these effects in a minimal axio-dilaton system which has been studied in cosmological settings in various forms in [58–67], consisting of a dilaton χ conformally coupled to matter and its partnered axion field \mathbf{a} whose kinetic term carries a χ -dependent prefactor $W^2(\chi)$. The resulting curved field space induces a characteristic two-derivative interaction, proportional to $W(\chi)W_{,\chi}(\chi)\mathbf{a}'(r)^2$, which acts as a source term in the dilaton equation of motion. As a result, axion gradients generically backreact on the dilaton profile even in the absence of direct potential couplings.

The physical effect on the dilaton's evolution depends largely on the sign of $W_{,\chi}$. Given that the dilaton always rolls asymptotically to infinity in the vacuum exterior to a body, if positive, the axion gradient further sources the dilaton and induces a localised dilaton profile wherever it is present. This modifies *where* the dilaton can evolve appreciably and so gives rise to very different profiles compared to where the dilaton would evolve naturally due to its matter coupling alone. In the vacuum exterior to astrophysical bodies a light dilaton will always evolve radially along a Yukawa tail towards its environmental value χ_{env} according to

$$\chi \simeq \chi_{\text{env}} - \frac{L}{r}, \quad (1)$$

where the parameter L is the scalar charge of the dilaton and its size controls the overall exterior spatial gradients associated with the field. We seek to answer if this external kinetic driving can generically reduce the dilaton's scalar charge exterior to objects (as reducing the scalar charge amounts to screening the dilaton), e.g. by displacing where the dilaton's evolution occurs, driving the dilaton between its asymptotic minima in a smaller radius (i.e. creating a thinner dilaton shell). We find that the kinetic driving cannot suppress the net scalar charge in any generic regime because of the additional charge penalty associated with adding an externally driven dilaton gradient to the system. However, if $W_{,\chi}$ is negative, the axion gradient generically acts to oppose the dilaton's single field motion towards large χ , and has been shown to reduce generically the dilaton's gradient and effective coupling at the surface of sources¹ [68]. This

occurs naturally when combining this effect with a global energy minimisation of the system, which is dynamically selected when the dilaton's surface and asymptotic value are free to vary, removing the need for fine-tuning.

We consider different case studies to illustrate the screening mechanisms in action in this paper, focusing on different variations of stringy dilatons for which the density-dependent effective potential admits minima. Whether local systems are pinned to these minima depends on the in-medium mass scale, and for a dark-energy dilaton the field typically remains unpinned on stellar and planetary scales. In this regime, attempts to screen by forcing a localised interpolation with an external field, i.e. a thin shell, are generically counterproductive, since displacing χ further from its environmental value without the possibility of reaching an asymptotic stationary point increases the total dilaton excursion and therefore the exterior scalar charge. Viable screening instead proceeds through dynamical gradient suppression when $W_{,\chi} < 0$, selected by the minimum-energy configuration of the coupled axio-dilaton system.

If the dilaton is sufficiently massive, or if the system is sufficiently dense, local objects become pinned to the in-medium minimum. In this case the gradient-suppression mechanism is generically frustrated from reaching the global equilibrium configuration. Reducing the exterior dilaton gradient using an additional field would then require displacing χ away from its minimum in some interior region, incurring an additional potential-energy cost. As a result, substantial screening in pinned environments depends sensitively on environmental details and typically requires tuning of the axion profile or model parameters rather than arising robustly from energy minimisation. Even when the axion kinetic coupling has the opposite sign $W_{,\chi} > 0$ and assists rather than opposes the dilaton's roll towards its exterior minimum, the resulting localisation of the transition into a thin shell does not suppress the fifth force. The axion gradient contributes its own charge penalty through the flux balance, so that reducing the shell width $\Delta R/R_s$ leaves the exterior charge L essentially unchanged, decoupling thin-shell formation from actual screening.

These results show that multi-field axio-dilaton dynamics qualitatively alter the connection between profile localisation and observable fifth forces, and motivate treating pinned and unpinned environments separately even within a fixed microscopic model. This paper develops the corresponding analytic criteria and validates them against fully coupled numerical solutions², identifying the regions of parameter space in which axio-dilaton models remain compatible with local constraints while retaining cosmological relevance. Surprisingly, we find that screening the dilaton in a multi-field context depends crucially on the sign of the kinetic contribution

¹ We shall use the shorthand BBQ for this procedure.

² The code used in this work is publicly available at [69].

of the axion to the dilaton's evolution. When negative, screening can be achieved when the dilaton's value inside matter is not pinned by its potential. Screening becomes a global property resulting from the minimisation of the scalar field energy. In this case too, screening for pinned fields follows the same pattern as in the single-field case, i.e. with a thin shell. This requires a tuned cancellation between the axion and dilaton contributions to the scalar charge. This has to be contrasted with the unpinned case where the dilaton adapts its value at the surface of a compact object and minimises the energy of the field configuration. On the contrary, when the sign of the kinetic coupling between the axion and the dilaton is positive, the minimisation procedure fails and the axion plays hardly any role in the thin shell mechanism.

The remainder of the paper is organised as follows. Section II introduces the general spherically symmetric multi-field setup and the scalar charge that controls fifth forces. Section III then defines the axio-dilaton system and its two-derivative field-space interactions. Section IV introduces the string dilaton and its model features, and then reviews the single-field dilaton and why thin-shell screening fails for constant coupling. Section V studies multi-field thin shells and shows that axion-driven localisation does not generically suppress the exterior scalar charge, i.e. screening requires a tuned cancellation between dilaton and axion contributions to the scalar charge. Section VI presents gradient suppression via energy minimisation (the BBQ mechanism) and identifies when it yields robust charge suppression, including in runaway/no-minimum cases. We revisit the implications for viable dilaton models on astrophysical scales in Section VII and finally conclude in Section VIII.

II. SPHERICALLY SYMMETRIC SYSTEMS

General setup and motivation

We begin with a general scalar-tensor theory in the Einstein frame (minimally coupled to the Ricci scalar R), containing N scalar fields ϕ^I with target-space metric $G_{IJ}(\phi^K)$, a potential $V(\phi^I)$, and a conformal coupling $A(\phi^I)$ to matter,

$$S = \frac{1}{2} \int d^4x \sqrt{-g} \left[M_{\text{pl}}^2 R - G_{IJ}(\phi^K) \partial_\mu \phi^I \partial^\mu \phi^J - 2V(\phi^I) \right] + S_m[A^2(\phi^I) g_{\mu\nu}, \psi_m], \quad (2)$$

where ψ_m denotes the matter fields and M_{pl} is the reduced Planck mass.

Much of the literature on scalar-tensor screening focuses on single-field models, but this focus turns out to be overly restrictive from the point of view of effective field theory. As emphasised in Refs. [70–73], the leading interactions that survive at low energies (once dangerous zero-derivative potential terms are suppressed by

symmetries [70, 74, 75]) are the two-derivative σ -model interactions

$$\mathcal{L}_{2\text{deriv}} = \frac{1}{2} \sqrt{-g} \left[M_{\text{pl}}^2 R - G_{IJ}(\phi^K) \partial_\mu \phi^I \partial^\mu \phi^J \right]. \quad (3)$$

These interactions are generically expected to compete with the two-derivative sector of GR at astrophysical and cosmological energies.

Crucially, these kinetic-metric interactions have *no physical effect* when the target space is one-dimensional: every one-dimensional manifold is locally flat, so for a single scalar field the metric can always be removed by a field redefinition. This means that single-field screening models accidentally eliminate the entire class of two-derivative σ -model interactions. In such models all non-trivial dynamics must come from potentials or matter couplings, with the kinetic sector playing no role. From the EFT point of view this is highly nongeneric. Fundamental UV theories with symmetries built in *predict* that the kinetic geometry is the dominant source of scalar interactions in the infrared.

For multiple fields the situation changes qualitatively. A curved target space necessarily introduces Christoffel symbols $\Gamma^I_{JK}(\phi)$ which appear in the field equations as genuine two-derivative forces. Specialising eq. (2) to static, spherically symmetric configurations $\phi^I = \phi^I(r)$ and varying with respect to $\phi^I(r)$ gives

$$\frac{1}{r^2} \frac{d}{dr} (r^2 G_{IJ} \phi^{J'}) - \frac{1}{2} \partial_I G_{JK} \phi^{J'} \phi^{K'} = \partial_I V + \partial_I A \rho_m(r), \quad (4)$$

where a prime denotes d/dr and $\rho_m(r)$ denotes the conserved matter density. The geometric term

$$\frac{1}{2} \partial_I G_{JK} \phi^{J'} \phi^{K'}, \quad (5)$$

acts as an effective source for ϕ^I whenever another field has a spatial gradient. This contribution is purely two-derivative and it persists even when the second field enjoys an exact shift symmetry. As a result, multi-field systems can exhibit low-energy behaviour that has no counterpart in any single-field reduction.

Because UV-complete theories generically contain several light scalar fields, and because their low-energy interactions are governed by the curved geometry of $G_{IJ}(\phi^K)$, the dynamics of any one field are almost never isolated in practice [76, 77]. Field-space interactions and turning trajectories couple adiabatic and entropic directions, so gradients or fluctuations of one scalar can generically source, drag, or obstruct the rolling of another [78–80]. Consequently, single-field screening models omit precisely the class of interactions that fundamental theory says should be present, and are therefore likely to be qualitatively inaccurate descriptions of well-motivated scalar-tensor physics.³

³ Unless the additional fields are consistently decoupled or integrated out within a controlled effective theory [81, 82]

The next section seeks to illustrate this point explicitly using the case study of axio-dilaton systems, but first we introduce the appropriate machinery for studying these effects within astrophysical settings.

The scalar charge

We focus on a single light field ϕ whose scalar force on compact objects is calculated below. This scalar interacts with other scalars via the kinetic couplings appearing in the Klein-Gordon equation (4). For a static, spherically symmetric configuration of this light scalar $\phi = \phi(r)$ in an approximately homogeneous environment, the solution exterior to a dense body of mass M and radius R_s at radii $r \gtrsim R_s$ takes the usual Yukawa/Laplace form

$$\phi(r) = \phi_{\text{env}} - \frac{L_\phi}{r} e^{-m_{\text{env}}(r-R_s)}, \quad (r \gtrsim R_s), \quad (6)$$

where ϕ_{env} is the environmental value of the field at large distances from the source, which reduces to

$$\phi \simeq \phi_{\text{env}} - \frac{L_\phi}{r}, \quad (7)$$

when $m_{\text{env}}(r-R_s) \ll 1$, where m_{env} is the environmental mass of the scalar. The constant L_ϕ , called the scalar charge, is conserved exterior to the body

$$L_\phi \equiv r^2 \phi'|_{r > R_s}. \quad (8)$$

It is the amplitude of the exterior tail and therefore controls the long-range fifth force. This solution is valid as long as the scalar potential can be neglected in the vicinity of the compact object. This is the case for instance when the scalar field acts as dark energy.

To connect L_ϕ to the interior dynamics, we specialise eq. (4) to the canonically normalised single-field equation of motion for ϕ in the Einstein frame,

$$\frac{1}{r^2} \frac{d}{dr} (r^2 \phi') = \partial_\phi V(\phi^I) + \partial_\phi A(\phi^I) \rho_m(r) + \frac{1}{2} \partial_\phi G_{JK}(\phi^I) \phi^{J'} \phi^{K'}. \quad (9)$$

Integrating eq. (9) from 0 to ∞ and using regularity at the origin ($r^2 \phi' \rightarrow 0$ as $r \rightarrow 0$), together with the exterior tail eq. (8), gives the flux/charge relation

$$L_\phi = \int_0^\infty dr r^2 [V_{,\phi}(\phi^I) + A_{,\phi}(\phi^I) \rho_m(r) + \frac{1}{2} \partial_\phi G_{JK}(\phi^I) \phi^{J'}(r) \phi^{K'}(r)]. \quad (10)$$

The exterior charge is therefore an integrated measure of all sources for ϕ across the configuration. Potential gradients and matter couplings contribute, as well as σ -model interactions encoded in $\partial_\phi G_{JK} \phi^{J'} \phi^{K'}$. Cancellations among these terms can suppress L_ϕ even when the fields vary non-trivially inside/outside the object.

If ϕ is the only scalar that couples to the matter species, matter follows geodesics of $\tilde{g}_{\mu\nu} = A^2(\phi)g_{\mu\nu}$, so a test body experiences an acceleration due to the scalar ϕ given by

$$a_\phi = -\nabla \ln A(\phi) = -\frac{\beta_{\text{env}}}{M_{\text{pl}}} \nabla \phi, \quad \frac{\beta_{\text{env}}(\phi_{\text{env}})}{M_{\text{pl}}} \equiv \left. \frac{d \ln A}{d\phi} \right|_{\phi_{\text{env}}}. \quad (11)$$

This is the case, for instance, when all the fields but ϕ are pseudo-Goldstone bosons with no non-derivative interactions to matter. For a light field on solar-system scales, the exterior tail eq. (7) implies

$$|a_\phi| \simeq \frac{\beta_{\text{env}}}{M_{\text{pl}}} \frac{L_\phi}{r^2}, \quad (r \gtrsim R_s), \quad (12)$$

so the scalar force falls off as $1/r^2$, just like Newtonian gravity,

$$|a_N| = \frac{G_N M}{r^2} = \frac{\Phi_N(R_s) R_s}{r^2}, \quad \Phi_N(R_s) \equiv \frac{GM}{R_s}. \quad (13)$$

It is therefore convenient to parametrise the amplitude of the exterior scalar tail by introducing an effective coupling β_{eff} through

$$\frac{|a_\phi|}{|a_N|} \equiv 2 \beta_{\text{env}} \beta_{\text{eff}} \quad (m_{\text{env}} r \ll 1), \quad (14)$$

which, upon using the expressions above, is equivalent to the charge definition

$$L_\phi \equiv 2 \beta_{\text{eff}} M_{\text{pl}} \Phi_N(R_s) R_s. \quad (15)$$

With this definition, the unscreened limit corresponds to $\beta_{\text{eff}} \simeq \beta_{\text{env}} \simeq \beta$, giving the familiar force ratio $|a_\phi|/|a_N| \simeq 2\beta^2$.

For a given source there is therefore a direct correspondence between a scalar's exterior charge and its effective coupling strength to matter

$$\frac{L_\phi}{L_0} = \frac{\beta_{\text{eff}}}{\beta_{\text{env}}}, \quad (16)$$

where L_0 is the unscreened scalar charge. Screening a scalar therefore corresponds to reducing its net exterior charge. We now introduce two methods of suppressing L_ϕ in practice.

Screening mechanisms of interest

1. Thin shells

Thin-shell screening is the standard way a matter-coupled scalar evades local fifth-force bounds when its effective potential

$$V_{\text{eff}}(\phi; \rho_m) = V(\phi) + A(\phi) \rho_m, \quad (17)$$

admits density-dependent stationary points [50, 83–85]. For a spherical body with interior density ρ_c and exterior environmental density ρ_{env} , the field sits near an interior value $\phi_c \simeq \phi_{\text{min}}(\rho_c)$ throughout most of the volume until a rolling radius R_{roll} and transitions to the ambient value $\phi_{\text{env}} \simeq \phi_{\text{min}}(\rho_{\text{env}})$ only in a surface layer of thickness $\Delta R = R_s - R_{\text{roll}}$. When the scalar is light on the exterior scales probed by gravitational tests, the profile matches onto the Yukawa tail eq. (7), so the observable fifth force is controlled by the exterior charge eq. (8).

In the thin-shell regime the charge is sourced only by the small fraction of mass lying in the rolling layer, yielding the familiar scaling

$$\beta_{\text{eff}} \simeq 3\beta_{\text{env}} \frac{\Delta R}{R_s}, \quad \frac{L}{L_0} \simeq 3 \frac{\Delta R}{R_s}. \quad (18)$$

The usual thin-shell condition therefore amounts to $\Delta R/R_s \ll 1$, which is reviewed (and shown to fail) for the single-field dilaton in Section IV B. A key theme of this paper is that this relationship between a geometrically thin shell and the exterior charge is only true in an idealised single-field model. Once two-derivative field-space interactions contribute to eq. (10), shell localisation and fifth-force suppression become independent quantities (see Section V).

2. BBQ Screening

A different route to screening is possible when the shell picture itself is not well defined, either because V_{eff} has no relevant density-dependent minima or because the scalar is too light to relax to them on the scale of the source ($m_{\text{eff}}(\rho_c)R_s \ll 1$). In this regime $\phi(r)$ can roll throughout the interior and one should expect $\Delta R/R_s \sim 1$. Nevertheless, the fifth force can still be suppressed if the static configuration dynamically selects a surface value that minimises the total energy, which also happens to reduce the exterior gradient energy $\sim L_\phi^2/R_s$ and hence the conserved charge. We refer to this energy-selected charge suppression as the BBQ mechanism (following the minimisation logic of [68]).

In multi-field systems this becomes possible because the gradient energy of one field can depend on another through the target-space metric $G_{IJ}(\phi)$, and the same curved field-space structure contributes directly to the charge integral through the σ -model term in eq. (10). For the sign choices in which these two-derivative interactions can oppose the matter-induced source for the field of interest, the minimum-energy configuration can dynamically suppress the exterior charge L_ϕ even when no thin-shell forms [86]. This is the organising principle for the runaway/unpinned analyses in Section VI.

We now proceed to specifying the system of interest in this paper and begin applying the astrophysical toolkit laid out in this section.

III. MULTI-FIELD AXIO-DILATON SYSTEMS

The considerations above suggest studying at least two scalar fields when analysing screening of fifth forces. Among the simplest and best-motivated examples are axio-dilaton systems, consisting of an axion \mathbf{a} and dilaton χ , specified in terms of the covariant language as

$$\phi^I = (\chi, \mathbf{a}), \quad G_{IJ} = \text{diag}(1, W^2(\chi)). \quad (19)$$

This means the full action for our setup has the form⁴

$$S = \int d^4x \sqrt{-g} \left\{ \frac{M_{\text{pl}}^2}{2} \left[R - \partial_\mu \chi \partial^\mu \chi - W^2(\chi) \partial_\mu \mathbf{a} \partial^\mu \mathbf{a} \right] - V(\chi, \mathbf{a}) \right\} + S_m(A^2(\chi) g_{\mu\nu}, \Psi_m), \quad (20)$$

so that χ is a canonically normalised dilaton with a universal coupling to the trace of the energy-momentum tensor (through $A(\chi)$), while the axion \mathbf{a} is a shift-symmetric pseudoscalar whose two-derivative term is multiplied by a dilaton-dependent prefactor $W^2(\chi)$. In ultraviolet completions where χ and \mathbf{a} form a supersymmetric pair, $W(\chi)$ is not an arbitrary function but is fixed by the geometry of the scalar manifold, i.e. by the field-space metric inherited from the Kähler potential [87, 88]. A widely used and well-motivated parameterisation is the exponential form⁵

$$W(\chi) = W_0 e^{\zeta \chi}, \quad (21)$$

where ζ encodes the (constant) curvature scale of the two-dimensional target space [89–91]. The physical consequence of this curved field space is that axion gradients backreact on the dilaton through the connection term in the covariant equations of motion, yielding an effective source for χ .

For spherically symmetric and static configurations the field equations reduce to

$$\mathbf{a}'' + \frac{2}{r} \mathbf{a}' = -2 \frac{W_{,\chi}}{W} \chi' \mathbf{a}' + \frac{1}{W^2(\chi)} \left[\partial_{\mathbf{a}} V(\chi, \mathbf{a}) + \partial_{\mathbf{a}} U(\mathbf{a}) A(\chi) \rho_m(r) \right], \quad (22)$$

$$\chi'' + \frac{2}{r} \chi' = W(\chi) W_{,\chi}(\chi) \mathbf{a}'^2 + \partial_\chi V(\chi, \mathbf{a}) + \partial_\chi A(\chi) [1 + U(\mathbf{a})] \rho_m(r). \quad (23)$$

⁴ Unless explicitly stated otherwise we use fundamental units $c = \hbar = 1$ throughout and define the reduced Planck mass in terms of Newton's constant by $M_{\text{pl}}^{-2} = 8\pi G_{\text{N}}$.

⁵ We also consider quadratic functional forms for $W^2(\chi)$ in Section A to show the behaviour of the system and our conclusions remain robust in the presence of different kinetic coupling functional forms.

These equations exhibit explicitly the two-derivative interaction induced by the curved field space, where the axion sources χ only where $\mathbf{a}'(r) \neq 0$, and the strength of this source is controlled by the geometry through $WW_{,\chi}$.

The dilaton charge analogue of eq. (10) controlling the coupling strength of the dilaton to matter in this system is given by

$$L = [r^2 \chi'(r)]_0^\infty = \int_0^\infty dr r^2 [WW_{,\chi} \mathbf{a}'(r)^2 + V_{,\chi} + A_{,\chi} \rho_m], \quad (24)$$

where ρ_m is the matter density. Finding a way to suppress this charge, either by suppressing contributions or identifying natural regimes where they largely cancel is the purpose of this paper.

Dilatons in the literature

To place this model in context, it is useful to recall that “dilaton” originally denotes the (pseudo-)Goldstone boson of broken scale invariance [59, 92–95], while in much of the scalar–tensor and string–moduli literature it is used more broadly, often as an umbrella term for light moduli whose variations induce an (approximately) universal conformal rescaling of the matter sector [40–42, 96–98]. Across this literature, the qualitative behaviour is largely dictated by three interrelated pieces of structure: the sign and magnitude of the matter coupling $\beta \equiv \partial \ln A / \partial \chi$, the slope of the underlying runaway potential for χ (often approximately exponential in the Einstein frame), and, in multi-field settings, the sign of the axion–dilaton kinetic coupling ζ which fixes the sign of $W_{,\chi}$. These sign choices control whether the density-dependent effective potential for χ admits local minima (pinning the field in different environments) or instead remains runaway. With this motivation, we summarise in Table I the main dilaton classes studied to date and the sign choices most commonly realised in each construction, for the dilaton’s potential

$$V = V_0 e^{\lambda \chi / M_{\text{Pl}}}, \quad (25)$$

and matter coupling function

$$A(\chi) = e^{\beta \chi / M_{\text{Pl}}}. \quad (26)$$

This serves as a map for the regimes analysed in the remainder of the paper.

The *string dilaton* corresponds to the gravi–dilaton actions studied in [47, 50, 96, 99]. By contrast, *yoga* models [59, 63, 68] arise when the axion is the imaginary partner of the volume modulus χ . Both cases typically predict $\beta \sim \mathcal{O}(0.1)$ couplings to matter. In yoga models the dilaton potential is engineered to possess a shallow vacuum minimum at the dark–energy scale, so that the field is asymptotically stabilised on cosmological scales. Adding matter shifts this minimum only weakly so that the density–dependent effective potential retains

a nearby minimum, but its curvature remains set by the dark–energy scale and is therefore far too small to pin the field in astrophysical environments. So although the dilaton is cosmologically stabilised it behaves as effectively unpinned around compact objects and a weakly fixed asymptotic value determined cosmologically.

Axions in the literature

The axion sector contains two contributions: a joint potential $V(\chi, \mathbf{a})$, typically periodic in the axion direction [100] as in ordinary axion models⁶, and a matter–induced coupling function $U(\mathbf{a})$ arising from the coupling to the Einstein-frame matter energy density

$$\rho_m E = A(\chi)(1 + U(\mathbf{a}))\rho_m(r), \quad (27)$$

where ρ_m is the conserved mass density and in what follows we assume $U(\mathbf{a}) \ll 1$. The two fields roll in their respective directions of the effective potential

$$V_{\text{eff}}(\chi, \mathbf{a}; \rho_m) = V(\chi, \mathbf{a}) + [1 + U(\mathbf{a})]\rho_m(r)A(\chi), \quad (28)$$

whose density–dependent stationary points determine the asymptotic interior and exterior values of \mathbf{a} in regions of approximately constant density. The interior and exterior equilibrium values

$$\mathbf{a}_- \equiv \mathbf{a}(r = 0), \quad \mathbf{a}_+ \equiv \mathbf{a}(r \gg R_s), \quad (29)$$

are obtained from the local force–balance relation $\partial_{\mathbf{a}} V_{\text{eff}} = 0$ evaluated at the interior density ρ_c and the exterior density ρ_{env} . These definitions rely only on the existence of local stationary points and do not assume any particular microphysical form for V or U . In general the axion force–balance condition defines a density–dependent valley $\mathbf{a}_*(\chi; \rho)$ in field space.

The thin–shell estimates below assume that the axion transition is much more localised than the dilaton transition. This implies the axion should be heavy on the scale of the object so that it interpolates only in a narrow surface band,

$$\ell_a \sim m_{a,\text{sh}}^{-1} \ll \Delta R \lesssim R_s, \quad (30)$$

where $m_{a,\text{sh}}$ is the axion effective mass in the surface/transition region. In this regime $\mathbf{a}'(r)$ has support only very close to $r \simeq R_s$, so the axion backreaction term acts as a near–surface kick in the dilaton equation rather than an extended source.

This scale hierarchy is illustrated in Figure 1. In the middle panel, the case corresponding to a heavier axion inside the source (orange) shows an axion interpolation confined to a thin layer near the surface, whereas for

⁶ Although axions with exact quadratic potentials can be found in dual axion frameworks [101]

Model	β	λ	Thin Shell	BBQ, unpinned	BBQ, pinned
			$(W_{,\chi} > 0)$	$(W_{,\chi} < 0, m_{\text{eff}} R_s \ll 1)$	$(W_{,\chi} < 0, m_{\text{eff}} R_s \gg 1)$
String Dilaton	> 0	< 0	No	Yes	Environmentally fine-tuned
Yoga	< 0	< 0	No	Yes	–

TABLE I: Summary of different dilaton models and the signs of their couplings to the standard model particles, β , and potential slopes, λ , given in eqs. (25) and (26). Dilatons with opposite sign β and λ exhibit minima in their effective potentials, while those with identical signs do not. We distinguish the BBQ regime ($W_{,\chi} < 0$) into an *unpinned* case ($m_{\text{eff}} R_s \ll 1$) and a *pinned* case ($m_{\text{eff}} R_s \gg 1$).

a lighter axion (blue) the axion varies over $\mathcal{O}(R_s)$ and its gradients persist well away from $r \simeq R_s$. The top panel shows the consequence for the dilaton: when the axion gradient is localised χ remains close to its interior value until near the surface, but when the axion is light ($m_{a,\text{sh}} R_s \lesssim 1$, blue) the same two-derivative coupling drives χ off its interior plateau well before $r \simeq R_s$. The usual thin-shell assumption that χ stays approximately stationary until a radius close to the surface is therefore not self-consistent in this regime.⁷

When the axion is heavy on macroscopic scales one may integrate it out. For fixed (χ, ρ_m) the axion rapidly relaxes to $\mathbf{a}_*(\chi; \rho_m)$, defined by

$$\partial_{\mathbf{a}} V_{\text{eff}}(\chi, \mathbf{a}; \rho_m) \Big|_{\mathbf{a}=\mathbf{a}_*} = 0, \quad (31)$$

which yields a reduced one-field effective potential

$$V_{\text{eff}}^{\text{red}}(\chi; \rho_m) \equiv V_{\text{eff}}(\chi, \mathbf{a}_*(\chi; \rho_m); \rho_m), \quad (32)$$

for the light dilaton to evolve in. This forms the basis of the analytic investigations conducted in Sections V and VI

Piecewise linear axion profile

To determine how an axion gradient modifies the usual dilaton profile in the analytic approximations used below, we adopt a representative piecewise linear axion profile. This can be seen as a leading-order Taylor expansion of the axion gradient around a very steep transition localised close to the surface of the object. The axion must interpolate between its interior and exterior equilibrium values set by the density-dependent effective potential eq. (28), and for understanding its effects on other light scalars, all that matters is the total jump $\Delta \mathbf{a} = \mathbf{a}_+ - \mathbf{a}_-$ and the width ℓ_a of the region in which $\mathbf{a}'(r)$ is nonzero.

This motivates the effective ramp

$$\mathbf{a}(r) = \begin{cases} \mathbf{a}_-, & r < \alpha R_s, \\ \mathbf{a}_- + (\Delta \mathbf{a} / \ell_a)(r - \alpha R_s), & \alpha R_s < r < R_s, \\ \mathbf{a}_+, & r > R_s, \end{cases} \quad (33)$$

with $\ell_a = (1 - \alpha)R_s$ and $\alpha \in [0, 1]$. Here ℓ_a is the characteristic width of the ramp, which would correspond to the inverse Compton wavelength of the axion, $\lambda_a \sim 1/m_{a,\text{in}}$, in the transition region between the interior and exterior of the object, where $m_{a,\text{in}}(r)$ is the interior mass of the axion.

In practice, axion profiles of this type can be realised using relatively simple microphysical potentials. In the full two-field numerical analysis presented below, we adopt separable forms for the scalar potentials,

$$V(\chi, \mathbf{a}) = V_\chi(\chi) + V_{\mathbf{a}}(\mathbf{a}), \quad (34)$$

with an axion vacuum potential

$$V_{\mathbf{a}}(\mathbf{a}) = \frac{1}{2} m_a^2 (\mathbf{a} - \mathbf{a}_+)^2, \quad (35)$$

and a matter-induced coupling function

$$U(\mathbf{a}) = \frac{1}{2} \frac{(\mathbf{a} - \mathbf{a}_-)^2}{\Lambda_a^2}. \quad (36)$$

In this setup, the vacuum contribution favours the minimum at \mathbf{a}_+ , while the matter coupling shifts the effective minimum towards \mathbf{a}_- in regions of sufficiently high density. The axion therefore interpolates between \mathbf{a}_+ and \mathbf{a}_- depending on whether the vacuum or matter contributions dominate the effective potential. The detailed shape and width of this transition are controlled by the microscopic vacuum mass m_a and the matter-coupling scale Λ_a . These functions can be viewed as leading order Taylor expansions around minima of the potentials.

Having introduced generic axio-dilaton models and the phenomenology of the respective fields, we now dive into the parameter choices and models specifics for string dilatons.

⁷ We treat the breakdown of the mass hierarchy between the axion and dilaton explicitly in the fully coupled numerical solutions of Section V.

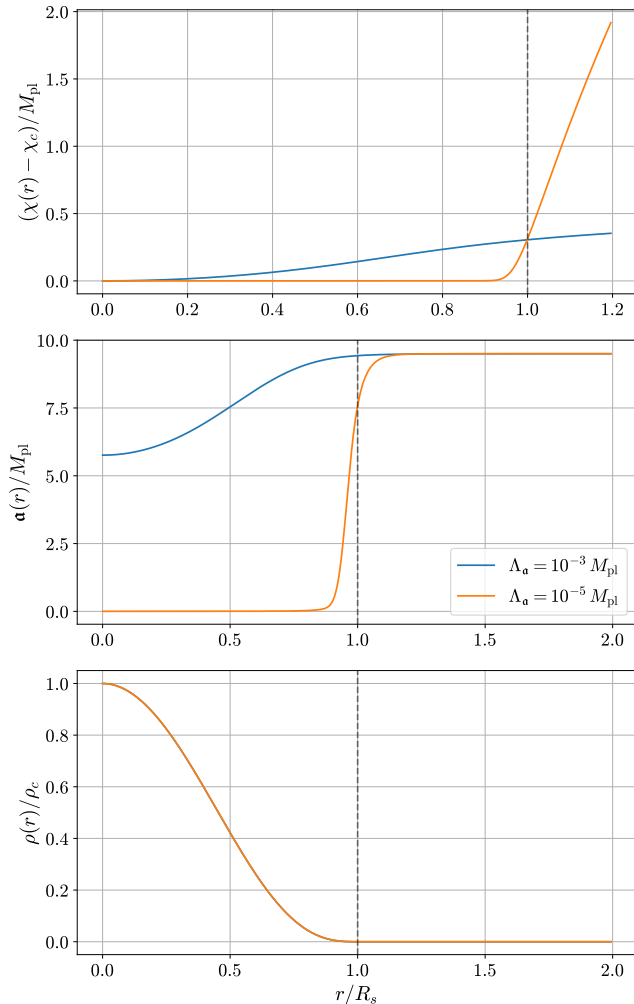


FIG. 1: Axion–dilaton profiles illustrating the scale hierarchy underlying the thin–shell approximation. **Top:** dilaton displacement; **middle:** axion; **bottom:** conserved density profile. The dashed line marks the surface $r = R_s$. The two curves correspond to the cut–off scale in eq. (36) being $\Lambda_a = 10^{-3} M_{\text{pl}}$ (broad axion transition) and $\Lambda_a = 10^{-5} M_{\text{pl}}$ (surface–localised axion transition), showing how a macroscopic axion gradient drives χ well inside the object. In both cases, $W_0 = 1$, $\zeta = \sqrt{2}$, and the vacuum axion mass is taken to be $m_a = 5 \times 10^{-17} \text{eV}$.

IV. STRING DILATONS

A. The models

The purpose of this section is to analyse the case of a stringy dilaton, by which we refer to the environmentally dependent (runaway) dilaton scenarios of [46, 50] (see also the screening review [102]). In the Einstein frame, a conformal coupling $\tilde{g}_{\mu\nu} = A^2(\chi) g_{\mu\nu}$ introduced

in eq. (20) implies that non-relativistic matter acts as a χ -dependent source, so static configurations can be organised by an effective potential composed of both matter and vacuum contributions [102], as in eq. (17). For the toy constant-coupling choice

$$A(\chi) = e^{\beta\chi/M_{\text{pl}}}, \quad \beta = \text{const}, \quad (37)$$

and for a runaway dilaton potential of the form used in [50], $V(\chi) \propto A^4(\chi) e^{-\chi/M_{\text{pl}}}$, the Einstein-frame self-interaction reduces to an exponential,

$$V_\chi(\chi) = V_0 e^{(4\beta-1)\chi/M_{\text{pl}}}, \quad (38)$$

so that

$$V_{\text{eff}\chi}(\chi; \rho_m) = V_\chi(\chi) + A(\chi) \rho_m(r), \quad (39)$$

with ρ_m the conserved Einstein-frame matter density. For reference, in [50] the cosmological value of the coupling today is $\beta_{\text{cos}} \simeq 0.23$, so throughout we take $\beta = 0.2$ as a representative coupling before screening effects are included.

Because $\beta = 0.2$ implies $A(\chi)$ is growing, while $V(\chi)$ is shrinking, minimising $V_{\text{eff}\chi}$ yields two equilibrium values, χ_c and χ_{env} , corresponding to the core and exterior densities. A key subtlety is that the interior value of the dilaton is *not* guaranteed to ever reach the dense–matter minimum χ_c in all dense objects. Whether the field can relax to χ_c within a finite object depends on the local curvature of the effective potential.

The pinned regime requires the effective mass, defined as

$$m_{\text{eff}}(\rho_m) \equiv \frac{\partial^2 V_{\text{eff}\chi}}{\partial \chi^2}, \quad (40)$$

to satisfy

$$\text{Pinned :} \quad m_{\text{eff}}(\rho_c) R_s \gtrsim 1. \quad (41)$$

For an ultralight dilaton with

$$\text{Unpinned :} \quad m_{\text{eff}}(\rho_c) R_s \ll 1, \quad (42)$$

the field cannot track χ_c and remains close to χ_{env} throughout most of the interior, up to $\mathcal{O}(\Phi_N)$ perturbations. Numerically, $m_{\text{eff}}(\rho_c) R_s \gtrsim 1$ corresponds to $m_{\text{eff}} \gtrsim 2.8 \times 10^{-16} \text{eV}$ for the Sun ($R_\odot = 7.0 \times 10^8 \text{m}$), and $m_{\text{eff}} \gtrsim 3.1 \times 10^{-14} \text{eV}$ for the Earth ($R_\oplus = 6.4 \times 10^6 \text{m}$), showing they do not pin the dilaton if it is cosmologically light.⁸ By contrast, a dark-energy-like mass $m_{\text{eff}} \sim H_0 \sim 10^{-33} \text{eV}$ gives $m_{\text{eff}} R_\odot \sim 10^{-17} \ll 1$.

⁸ Neutron stars are an important exception: these stars are many orders of magnitude more dense, making the effective potential for the dilaton more steep, and one can have $m_{\text{eff}}(\rho_{\text{NS}}) R_{\text{NS}} \gtrsim 1$ even when the vacuum mass is cosmological. The field is then pinned in the interior and develops a thin–shell–type profile in a relativistic stellar background; see e.g. [103, 104].

Pinning for cosmologically light dilatons can nevertheless be realised in models where the effective potential is sufficiently steep in dense regions, so that the local minimum shifts substantially between vacuum and matter and the curvature $m_{\text{eff}}^2(\rho) = \partial_\chi^2 V_{\text{eff}}$ increases rapidly with density. In such scenarios the dilaton can remain light on cosmological scales while becoming comparatively heavy in high-density environments, and the appropriate screening mechanism is then selected dynamically by the local value of $m_{\text{eff}}(\rho)$.

A useful way to quantify the required potential steepness in dense regions is via the scaling of the curvature at the density-dependent minimum, $m_{\text{eff}}(\rho) \propto \rho^p$. Pinning on a length scale λ requires $m_{\text{eff}}(\rho) \gtrsim \lambda^{-1}$, and between two environments one has $m_{\text{eff}}(\rho_2)/m_{\text{eff}}(\rho_1) = (\rho_2/\rho_1)^p$. Given the enormous density contrast between cosmological and stellar/planetary environments, even moderate p can yield many orders-of-magnitude increases in m_{eff} . For example, $\rho_*/\rho_{\text{cos}} \sim 10^{29}$ implies $m_*/m_{\text{cos}} \sim 10^{10}$ for $p = 1/3$, while $p \simeq 1/2$ – $2/3$ gives $m_*/m_{\text{cos}} \sim 10^{15}$ – 10^{20} . In standard chameleon potentials $V \propto \chi^{-n}$ one finds $m_{\text{eff}}(\rho) \propto \rho^{(n+2)/[2(n+1)]}$ [102]. For the canonical chameleon case $n = 1$ with the potential scale fixed to the dark-energy value, recent laboratory (e.g. [105]) and fifth-force searches place extremely strong constraints, excluding essentially the entire cosmologically viable parameter space across a wide range of β . Larger values of n generally remain viable, but within restricted regions of the (β, n) parameter space [106, 107]. This means that pinning a cosmologically light scalar on Solar-System scales requires an exceptionally rapid growth of m_{eff} with density, leaving only small corners of chameleon-like parameter space (although increasing n does reopen viable regions).

Another important point to note about the upcoming analysis is the preceding discussion treats the environment through a single background value χ_{env} and thus implicitly assumes a separation of scales between compact objects and the larger-scale host potential. In the presence of strong non-linearities this need not be a reliable assumption. Overlapping non-linear regions leading to multi-source boundary conditions, and spatially varying screening efficiencies can modify the effective ambient value and the resulting exterior charge. A definitive assessment of the galactic/solar environment therefore requires either a dedicated many-body treatment or cosmological/galactic N-body simulations that resolve the coupled scalar dynamics.⁹ We do not attempt such a

calculation here, and instead adopt χ_{env} as an effective parameter encoding the local environment.

With all of these complications and caveats in mind we use the rest of this paper to see what scenarios work in practice with the screening mechanisms at hand for these types of scalars.

B. Thin-shell failure for a single field dilaton

Before analysing the full axio-dilaton system, it is useful to recall the standard behaviour of a single dilaton field coupled to matter.

In order to model the dynamics of the single field dilaton in the solar system, e.g. around a planet, we consider the dynamics of this two-field system in the presence of a uniform-density, spherically symmetric source of radius R_s and density $\rho_m(r < R_s) = \rho_c$, embedded in an exterior environment with density $\rho_m(r > R_s) = \rho_{\text{env}}$. If pinned, the dilaton will sit at the interior and exterior equilibrium values χ_c and χ_{env} of eq. (39) below and above the surface of the source, and for a thin shell to form, the field must interpolate between these values close to the source's surface, as discussed in Section II 1. Following the prescription in [50], for a spherical body with surface Newtonian potential $\Phi_N(R_s)$, the standard thin-shell condition can be evaluated as

$$\frac{\Delta R}{R_s} = \frac{|\chi_{\text{env}} - \chi_c|/M_{\text{pl}}}{3\beta\Phi_N(R_s)} \ll 1, \quad (43)$$

where $\Delta R = R_s - R_{\text{roll}}$ is the thickness of the layer in which the field departs from the interior value.

For the exponential coupling the field excursion evaluates to the well-known form

$$|\chi_{\text{env}} - \chi_c| \simeq \frac{M_{\text{pl}}}{1 - 3\beta} \left| \ln \frac{\rho_{\text{env}}}{\rho_c} \right|. \quad (44)$$

For any realistic density contrast, this excursion is extremely large. Since the denominator of eq. (43) is tiny for astrophysical objects ($\Phi_N \sim 10^{-6}$ for the Sun), the ratio in eq. (43) satisfies

$$\frac{\Delta R}{R_s} \gg \mathcal{O}(1), \quad (45)$$

and no thin shell forms.

As a consequence of eq. (18), the scalar force mediated by χ remains unscreened and has strength $\sim \beta^2$ relative to gravity. Compatibility with solar-system tests therefore requires $\beta \lesssim 10^{-3}$, making the single-field dilaton effectively inert. This constitutes the robust no-go theorem for dilaton screening with constant coupling [114].

The failure of the single-field dilaton is not unsurprising. As emphasised in Section II, single-field models remove the geometric σ -model interactions that generically dominate multi-field low-energy dynamics. We now show explicitly how the presence of a second heavy field (an axion with a field-dependent kinetic prefactor) modifies the shell balance and qualitatively alters the screening behaviour.

⁹ Nonlinear screening in scalar-tensor theories has been widely studied using modified-gravity N -body simulations that evolve the scalar field alongside the matter distribution; see for example [108–113]. These simulations primarily focus on large-scale structure and dark-matter halo formation on cosmological scales, while simulations resolving the scalar field profiles of stellar-scale compact objects embedded in realistic galactic environments remain largely unexplored.

V. MULTI-FIELD THIN-SHELLS (WITH $W_{,\chi} > 0$)

A. Axions and their effects

We now turn to accounting for the deviations in the shell profile and charge-shell radius relation in the presence of the dilaton's partnered axion field. In this case, the interior and exterior dilaton values χ_c and χ_{env} are minima of the reduced effective potential eq. (32), which depends on the equilibrium values \mathbf{a}_+ and \mathbf{a}_- , with \mathbf{a}_\pm determined by the force-balance condition eq. (31) and the full effective potential eq. (28).

As discussed in Section III, in the parameter regime of analytical interest here the axion is heavier than the dilaton on macroscopic scales, so that the ramp is localised in a narrow region close to the surface,

$$\ell_a \ll \Delta R. \quad (46)$$

Consequently, the axion gradient contributes to the dilaton equation of motion only through a near-surface source localised within the ramp, and its effect is controlled by the ramp data $(\Delta \mathbf{a}, \ell_a)$. In this region, the axion gradient gives the dilaton a near-surface kick in χ' whose direction is determined by $WW_{,\chi}$, as seen in eq. (23). We focus to start with on the case of $W_{,\chi}\chi'(r) > 0$, corresponding to the axion driving being the same sign as the dilaton's velocity, further accelerating the dilaton and driving it between its minima more efficiently, in turn reducing the dilaton's shell width.

The multi-field thin-shell analysis in this case reduces to evaluating the integrated version of eq. (23) across $[R_{\text{roll}}, R_s]$. Multiplying eq. (23) by r^2 and integrating only across the region where χ rolls, the left-hand side is a total derivative equivalent to the dilaton charge,

$$L = \int_{R_{\text{roll}}}^{R_s} dr \frac{d}{dr} [r^2 \chi'(r)] = [r^2 \chi'(r)]_{R_{\text{roll}}}^{R_s} \simeq \frac{R_s^2}{\Delta R} \Delta \chi, \quad (47)$$

where we used the thin-shell approximation $r \simeq R_s$ throughout the layer and the no-roll condition outside the shell $\chi'(R_{\text{roll}}) = 0$. The integrated equation yields the global shell balance relation

$$\int_{R_{\text{roll}}}^{R_s} r^2 V_{,\chi} dr + \int_{R_{\text{roll}}}^{R_s} r^2 A_{,\chi} \rho_m dr + \int_{R_{\text{roll}}}^{R_s} r^2 WW_{,\chi} \mathbf{a}'^2 dr = L. \quad (48)$$

We now evaluate each term in the thin-shell regime, where all non-vanishing support is restricted to narrow intervals near $r \simeq R_s$.

a. Axion-gradient (overlap) integral. Since the heavy axion's profile is thin compared with R_s , we set $r \simeq R_s$ throughout its support, and any slowly varying function of χ can be evaluated at the surface value $\chi_s \equiv \chi(R_s)$ up to fractional corrections $\mathcal{O}(\ell_a/R_s)$. This

gives

$$\begin{aligned} \int_{R_{\text{roll}}}^{R_s} r^2 WW_{,\chi} \mathbf{a}'^2 dr &\simeq R_s^2 \left(\frac{\Delta \mathbf{a}}{\ell_a} \right)^2 \int_{\alpha R_s}^{R_s} dr WW_{,\chi}(\chi(r)) \\ &\simeq R_s^2 \left(\frac{\Delta \mathbf{a}}{\ell_a} \right)^2 WW_{,\chi}(\chi_s) \ell_a. \end{aligned} \quad (49)$$

The sign of $WW_{,\chi}(\chi_s) \propto \zeta$ therefore directly controls whether the overlap term behaves as an effective stiffness ($W_{,\chi}(\chi_s) < 0$) or an assisting drive ($W_{,\chi}(\chi_s) > 0$).

b. Potential-slope integral. We decompose the potential slope into the usual single-field driving piece and a genuine multi-field correction,

$$V_{,\chi}(\chi, \mathbf{a}) = V_{,\chi}(\chi_c, \mathbf{a}_-) + [V_{,\chi}(\chi, \mathbf{a}) - V_{,\chi}(\chi_c, \mathbf{a}_-)]. \quad (50)$$

The first term is the standard single-field contribution that drives the dilaton across the shell of width ΔR , while the second measures the departure from the single-field case and is non-negligible only within the overlap with the axion gradient, where both fields depart from their interior values.

Approximating $r \simeq R_s$ across both supports and evaluating slowly varying functions at the surface values $\chi_s \equiv \chi(R_s^-)$ and \mathbf{a}_+ gives

$$\begin{aligned} \int_{R_{\text{roll}}}^{R_s} r^2 V_{,\chi}(\chi, \mathbf{a}) dr &\simeq R_s^2 V_{,\chi}(\chi_c, \mathbf{a}_-) \Delta R \\ &\quad + R_s^2 \int_{\alpha R_s}^{R_s} dr [V_{,\chi}(\chi, \mathbf{a}) - V_{,\chi}(\chi_c, \mathbf{a}_-)] \\ &\simeq R_s^2 \left(V_{,\chi}(\chi_c, \mathbf{a}_-) \Delta R + [V_{,\chi}]_{\chi_c, \mathbf{a}_-}^{\chi_s, \mathbf{a}_+} \ell_a \right). \end{aligned} \quad (51)$$

This cleanly separates the usual single-field driving term from the gradient overlap correction induced by the axion ramp.

c. Matter-coupling integral. Across the thin layer the density can be treated as constant, $\rho_m(r) \simeq \rho_c$. This gives

$$\begin{aligned} \int_{R_{\text{roll}}}^{R_s} dr r^2 A_{,\chi}(\chi) \rho_m(r) &\simeq R_s^2 A_{,\chi}(\chi_s) \rho_c \Delta R \\ &= 6 A_{,\chi}(\chi_s) M_{\text{pl}}^2 \Phi_N(R_s) R_s \frac{\Delta R}{R_s}, \end{aligned} \quad (52)$$

where we used $\rho_c R_s^2 \simeq 6 M_{\text{pl}}^2 \Phi_N(R_s)$ to express the result in terms of the surface Newtonian potential of the dense object.

We note for later that the equations, eqs. (49) and (51) show that the multi-field modification is controlled by the axion's ramp profile $(\Delta \mathbf{a}/\ell_a)$, which differs from object to object, implying the axion modification to the dilaton dynamics has a generic dependence on object size and type. Because the axion sector is tied to the matter density and does not generically couple gravitationally (and

so universally) like the dilaton, composition can enter indirectly by shifting $\Delta\mathbf{a}$ and the effective ramp localisation, thereby inducing object-dependent environmental dynamics even when $A(\chi)$ is universal.

Charge and Shell profile relationships

The shell width can then be obtained by using the explicit evaluations eqs. (49), (51) and (52) in eq. (48), yielding

$$\frac{\Delta R}{R_s} \simeq \frac{2\Delta\chi - R_s \ell_a \left[\Delta V_{,\chi} + W(\chi_s) W_{,\chi}(\chi_s) \left(\frac{\Delta\mathbf{a}}{\ell_a} \right)^2 \right]}{6\beta M_{\text{pl}} \Phi_N(R_s) + R_s^2 V_{,\chi}(\chi_c, \mathbf{a}_-)}, \quad (53)$$

where

$$\Delta V_{,\chi} = V_{,\chi}(\chi_s, \mathbf{a}_+) - V_{,\chi}(\chi_c, \mathbf{a}_-).$$

Equation (53) has an intuitive physical explanation. When χ_c and χ_{env} are well-defined minima of the density-dependent effective potential, the total excursion $\Delta\chi$ is fixed. The axion contribution then modifies only how sharply the dilaton interpolates between these values near the surface. If the axion-induced contribution points in the same direction as the dilaton roll,

$$(WW_{,\chi})(\chi_s) \Delta\chi > 0, \quad (54)$$

then the ramp acts as an assisting source and the shell becomes narrower, reducing $\Delta R/R_s$. If the sign is opposite, the axion contribution opposes the roll and the shell must broaden to connect χ_c to χ_{env} . Thus in the minima-based pinned regime the axion renormalises the shell thickness by biasing the near-surface evolution through the two-derivative interaction $WW_{,\chi}(\mathbf{a}')^2$.

This effect is illustrated in Figure 2, where one can see the axion gradient driving the dilaton further and further towards its asymptotic value χ_{env} . At some point the axion can cause the dilaton to overshoot the asymptotic value, leaving a large residual offset between the field and χ_{env} at large radius.

Now we turn to see how this relates to screening. Assuming a thin shell using eq. (47) and that the dilaton approaches the Laplace tail exterior to the source as in eq. (1), one has

$$\frac{R_s}{\Delta R} (\chi_s - \chi_c) = \chi_{\text{env}} - \chi_s, \quad (55)$$

and hence the exterior charge can be evaluated to

$$L = R_s (\chi_s - \chi_{\text{env}}) = R_s \frac{\chi_c - \chi_{\text{env}}}{1 + \frac{\Delta R}{R}}, \quad (56)$$

which is independent of any explicit axion modification, and given that χ_c and χ_{env} are fixed minima of eq. (39) this means that the external charge is only influenced by

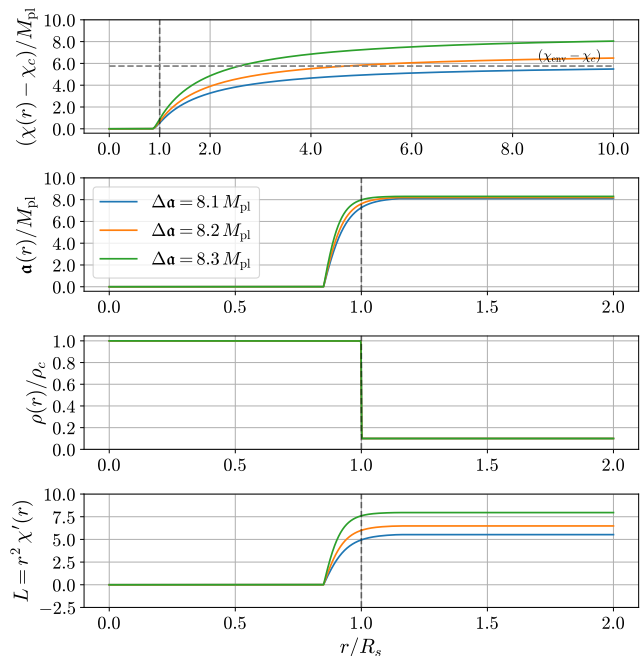


FIG. 2: Radial profiles (**First:** dilaton, **Second:** axion, **Third:** density, **Fourth:** dilaton charge) for different axion boundary jumps $\Delta\mathbf{a} = \mathbf{a}_+ - \mathbf{a}_-$ and a wide axion gradient using the flux conserving treatment for the axion described in Section B instead of solving the full equations of motion, with $\ell_a = 0.15$. Here we took $\beta = 0.2$, $\zeta = \sqrt{2}$ and $W_0 = 1$. We also took boundary conditions for the dilaton field $\chi'(0) = 0$, $\chi(0) = \chi_c$ corresponding to the pinned regime. Crucially for numerical stability in the presence of exponential factors of the dilaton field, we choose an Earth-like density $\rho_c \simeq 10^{-9} M_{\text{pl}}^2/R_s^2$, with $V_0 = 0.5 \rho_c$ and $\rho_{\text{env}} = 0.1 \rho_c$ (an unrealistically small hierarchy).

the axion through its effect on the shell width $\Delta R/R$, which is small by construction. This implies the axion sourcing has negligible effect on the external charge even if it drives the dilaton into the thin-shell configuration that the dilaton failed at doing on its own. This is because, while the axion is qualitatively pushing the dilaton into a more charge-suppressed configuration for the dilaton in isolation, this external axion gradient comes with its own charge sourcing on the dilaton through the coupling term in eq. (48), removing the ability for the net charge to be suppressed.

This is numerically confirmed in Figure 2 as well for wider axion ramps than the analytic approximations accommodate (showing the results do not change if this assumption is relaxed), where we can see in the bottom panel that driving the dilaton to its asymptotic value only changes the scalar charge by $\mathcal{O}(1)$ factors. It in fact increases the scalar charge as the shell width is made more thin, as predicted from eq. (56). The same effect is shown to occur for star-like density profiles in Figure 3,

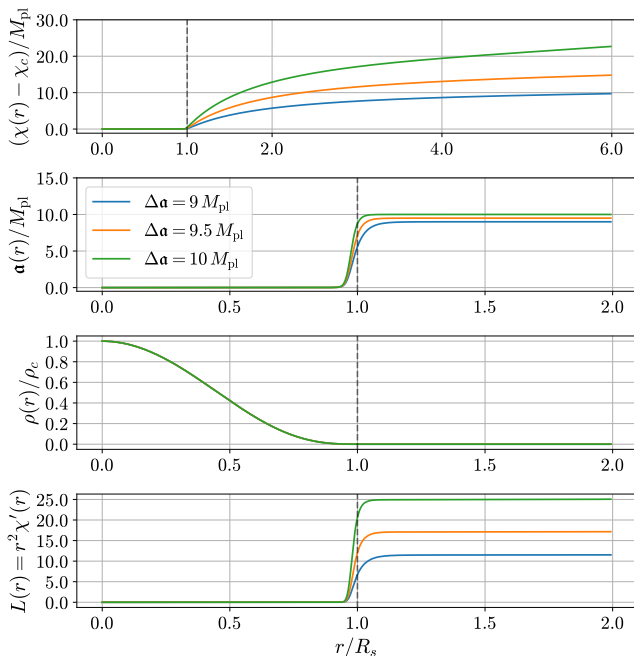


FIG. 3: Radial profiles for the same parameters as in Figure 2 except for $\rho_{\text{env}} = 10^{-8}\rho_c$ and a star-like object density profile described in Section B. In this case we solve the full multi-field equations using the microphysical parameters $\Lambda_a = 3 \times 10^{-6} M_{\text{pl}}$ and $m_a = 3 \times 10^{-16} \text{ eV}$.

showing that this result is robust across different density distribution and axion ramp effects. Sourcing the dilaton to make its transition close to the surface therefore allows for a thinner shell, but does not assist in any way with reducing its exterior charge.

B. Thin shell for ultra-light, unpinned dilatons

The thin-shell mechanism relies on the existence of two density-dependent equilibria of the dilaton effective potential, an interior value χ_c and an exterior value χ_{env} , between which the field interpolates within a parametrically thin surface layer. This picture breaks down when the dilaton is ultra-light on astrophysical scales.

For $m_\chi R_s \ll 1$, the dilaton cannot relax to a dense-matter equilibrium inside a finite object. Instead it stays close to the environmental value χ_{env} throughout the interior, with only $\mathcal{O}(\Phi_N)$ deviations, so there is no interior plateau and no parametrically thin rolling layer even in the single-field theory. The same effective behaviour is expected for yoga dilatons introduced in Section III, because although their potential has a shallow dark-energy minimum that fixes the asymptotic value cosmologically, its curvature remains far too small to pin the field in astrophysical environments, so one effectively has $m_{\text{eff}} R_s \ll 1$ and the thin-shell picture is not well

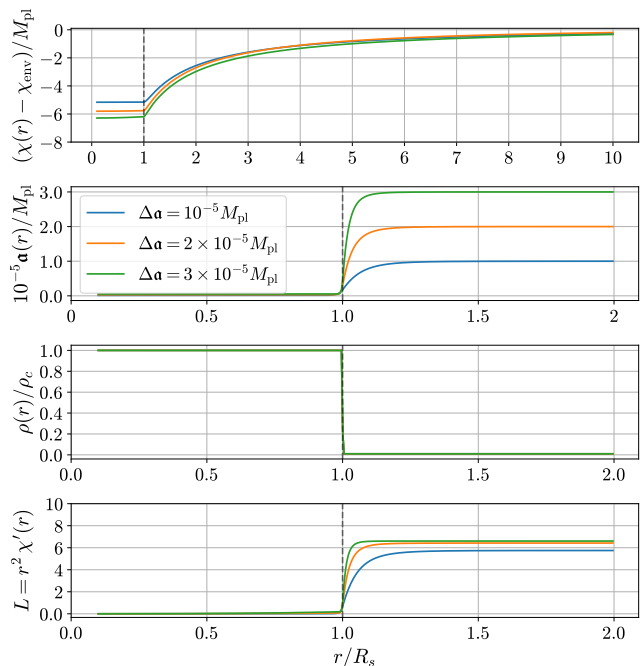


FIG. 4: Radial profiles for an unpinned dilaton with axion boundary jumps $\Delta a = a_+ - a_-$. We used the same parameters as Figure 2 but swapped a boundary condition at $\chi(0) = \chi_c$ with an asymptotic boundary condition $\chi(r_{\text{max}}) = \chi_{\text{env}}$. No parametrically thin rolling layer forms, consistent with $m_\chi R_s \ll 1$. Axion gradients modify the global profile rather than suppressing the exterior scalar charge.

defined.

This behaviour is illustrated in Figure 4. In this unpinned regime, localised axion gradients do not compress the radial width of the dilaton's transition. Rather, they modify the global dilaton profile, generically increasing the total field excursion and enhancing the exterior scalar charge L relative to the single-field case, as described by eq. (1).

Thin-shell screening therefore fails for ultra-light dilatons even in the presence of axion-induced near-surface dynamics. Screening in this regime must instead suppress the net scalar charge directly, rather than relying on geometric localisation of the profile.

In the next section we show that this is achieved by the BBQ mechanism, in which the axion backreaction dynamically selects a configuration that minimises the total energy and reduces the exterior charge.

VI. BBQ SCREENING: GRADIENT SUPPRESSION WHEN THE DILATON ROLLS FREELY (AND $W_{,\chi}(\chi_s) < 0$)

Having established that thin-shell screening of a light dilaton from solar system tests of gravity is seemingly not

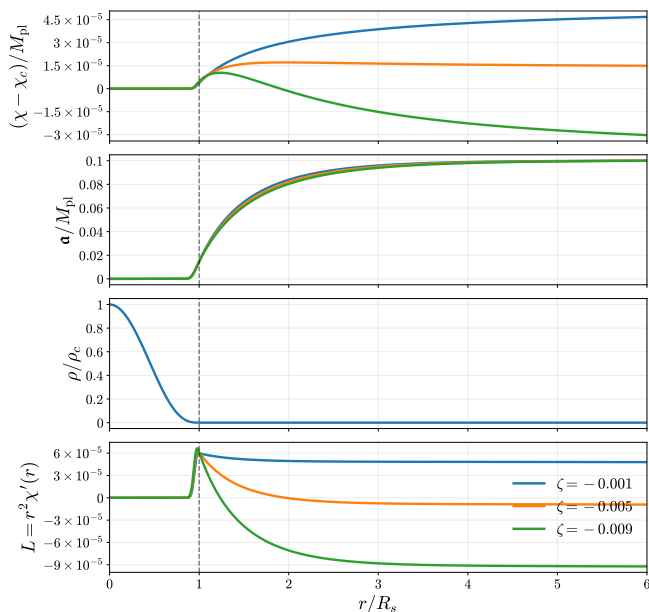


FIG. 5: Field profiles and dilaton charge evaluated for a pinned scalar in the presence of a suppressing coupling to the axion in a stellar density profile outlined in Section B. Here we took $W_0 = 1$, $V_0 = 10^{-5}\rho_c$ and $\rho_{\text{env}} = 10^{-15}\rho_c$. We solve the full coupled two-field system using the microphysical axion potentials eq. (36) and eq. (35) with $\Lambda_a = 3 \times 10^{-7} M_{\text{pl}}$ and $m_a = 3 \times 10^{-16} \text{ eV}$.

viable, regardless of pinning complexities in the multi-field context, we now focus on the opposite direction one can take. The next question to ask is what if instead the axion does something other than sourcing an additional dilaton profile? What happens if the axion is directly *suppressing* the dilaton’s gradient, further frustrating it from reaching its environmental minimum exterior to objects.

A. Pinned gradient suppression

Figure 5 illustrates the behaviour of the massive, pinned-dilaton system when the axion–dilaton kinetic coupling satisfies $W_{,\chi} \propto \zeta < 0$, inducing a negative sourcing contribution the dilaton’s Klein-Gordon eq. (23). In this case the axion gradient does not assist the dilaton in rolling towards its environmental minimum χ_{env} , but instead acts as an effective stiffness that opposes its motion. The resulting backreaction pushes the dilaton back up its exponential potential and flattens the exterior profile relative to the single-field expectation.

As shown in the bottom row of Figure 5, it is possible to tune the axion coupling such that this effect partially cancels the dilaton scalar charge, thereby reducing the associated fifth force. However, the figure already makes clear that this cancellation is highly delicate. A slightly

stronger coupling reverses the effect and instead enhances $|L|$, as the axion begins to drive the dilaton against its intrinsic rolling direction.

This behaviour can be understood directly from the global expression for the dilaton charge eq. (24), which shows that the exterior charge receives contributions from the potential slope, the matter coupling, and the axion–induced kinetic term. For $\zeta < 0$ the kinetic contribution can oppose the flux generated by the potential and matter terms near the surface. Achieving compatibility with solar-system bounds therefore requires these contributions to cancel at the level of at least three orders of magnitude, so that

$$\frac{L}{L_0} = \frac{\beta_{\text{eff}}}{\beta} \sim 10^{-3}. \quad (57)$$

The reason this cancellation is so finely tuned in the present setup is that the dilaton is massive and remains pinned close to the minimum of its effective potential throughout the interior of the object. Although dilaton gradients are energetically costly, displacing a heavy field away from this minimum incurs a large potential–energy penalty over the entire volume. The equilibrium configuration therefore necessarily contains an intrinsic surface gradient fixed by the mismatch between the interior and exterior minima. Any additional interaction, such as the axion kinetic coupling, must then be tuned independently to cancel this pre-existing flux across the configuration rather than being selected dynamically by energy minimisation.

In other words, the axion gradient is being used to counteract a surface gradient that is itself enforced by pinning. The cancellation required to suppress the charge is therefore accidental rather than structural, leaving little parametric room for successful screening. The very mechanism that renders the dilaton heavy and pinned is therefore also what obstructs robust gradient suppression.

As for how this relates to the discussion above and the apparent inconsistency that the axion can affect the exterior charge through eq. (24) while eq. (56) suggests that L is essentially axion-independent, the key point is that the thin-shell derivation implicitly assumes that the dilaton remains close to the minimum of its density-dependent effective potential throughout the interior and up to radii very near the surface. In the pinned thin-shell regime the intrinsic surface gradient is fixed by the mismatch between the interior and environmental minima, and the axion enters the shell analysis only as a perturbative modification of the near-surface dynamics, effectively renormalising the shell width $\Delta R/R_s$ while leaving the exterior charge controlled primarily by the fixed excursion $\chi_c - \chi_{\text{env}}$. By contrast, the regime in which $W_{,\chi} < 0$ suppresses the charge requires the axion contribution in eq. (24) to be comparable to the intrinsic flux generated by the potential and matter terms. Once this occurs the axion backreaction necessarily displaces the dilaton away from the effective minimum in

the near-surface region, so the field no longer tracks the pinned solution assumed in deriving eq. (56). The analytic thin-shell/minima expansion therefore ceases to be self-consistent in this regime. Charge suppression is then possible only through a cancellation among the different contributions to the global charge relation, which is inherently delicate and sensitive to the precise value of the axion coupling.

Environmentally-dependent screening

This tuning problem is exacerbated once one demands screening across multiple objects. An axion gradient tuned to cancel the dilaton's surface-generated flux for a given density profile will not generically cancel it with the same efficiency in another object with different $\rho_m(r)$, because the relative weighting of the terms in eq. (24) changes with the interior profile. This is illustrated in Figures 6 and 7, which choose the axion coupling ζ so that the exterior charge is strongly reduced ($L/L_0 \sim 10^{-3}$ far outside the source) for a solar-density source in blue, and then show this does not produce a comparable suppression for an otherwise identical star with $\rho_c = 0.1\rho_\odot$ in orange, which retains a much larger residual charge.

In a solar-system setting this lack of universality is fatal: satisfying solar constraints that probe the Sun's effective coupling (e.g. Shapiro time-delay bounds during solar conjunction) does therefore not ensure that other bodies are also screened. For example, if the Earth and Moon retain appreciable scalar charges, differential accelerations and equivalence-principle violations would be tightly constrained by lunar-laser-ranging [115, 116] and planetary-ephemeris tests [117, 118], regardless of whether the Sun itself has been tuned to be screened.

For this reason, axion-induced suppression of the dilaton charge is generically unnatural in the pinned regime. In the next section we instead consider light, unpinned dilatons, for which the surface value of the field is not fixed by a local minimum. In that case the axion backreaction can participate directly in the global energy minimisation of the configuration (because it is not so costly to displace the dilaton's interior value any more, energetically speaking), allowing charge suppression to arise dynamically rather than through fine-tuning object-by-object.

B. Un-pinned gradient suppression

The preceding section shows promise, and there is only one assumption being made that is neither realistic for a dark-energy-scale dilaton, nor helpful for screening: that the dilaton is pinned on astrophysical scales. Relaxing this assumption changes the screening picture entirely.

Doing so requires moving away from extremising the effective potential eq. (28) to define an equilibrium configuration, and instead allowing the surface and asymp-

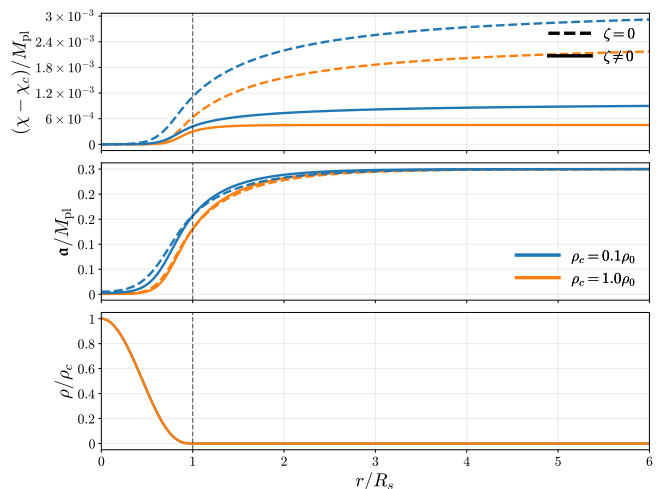


FIG. 6: Profiles of the constituent fields of the pinned dilaton system when the axion-dilaton coupling ζ has been tuned to cancel the dilaton gradient enough to satisfy solar system tests for a density distribution of the Sun in blue. The lines in orange show the profiles for exactly the same density distribution but 10% of the core density. Dashed lines show the corresponding $\zeta = 0$ cases for each. ρ_c is the core solar density and here we took $V_0 = 10^{-3}\rho_c$, $\rho_{\text{env}} = 10^{-15}\rho_c$, and $W_0 = 1$ and the two-field system was solved exactly with axion microphysical parameters $\Lambda_a = 3 \times 10^{-6}M_{\text{pl}}$ and $m_a = 3 \times 10^{-16}$ eV.

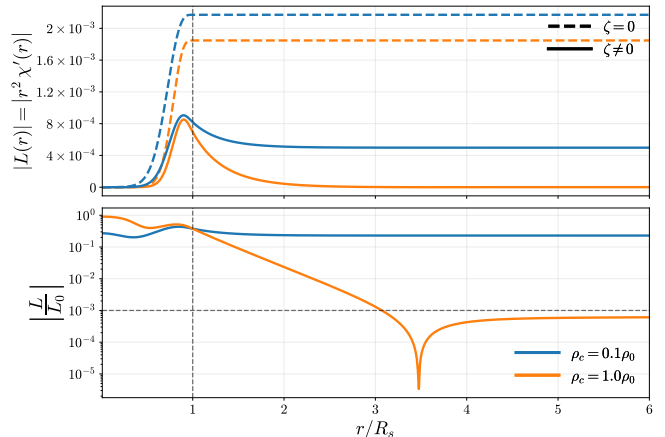


FIG. 7: **Top:** dilaton charge for the corresponding relevant profiles in Figure 6. **Bottom:** Charge relative to the unscreened charge L_0 obtained by running the simulation with $\zeta = 0$.

totic values to float. As emphasised in Ref. [50], screening can still occur when no such equilibria exist, and the relevant configuration is selected by minimising the total static energy subject to continuity of the field and its radial flux. This is precisely the mechanism already identified to work for yoga dilatons, and here we gener-

alise the narrow-width (infinitely sharp) axion-gradient treatment to finite-width (but still thin compared to the dilaton) linear ramps and fully coupled numerical solutions to compare with the regimes above.

C. Global scalar charge

Outside the source the dilaton satisfies the Laplace equation and takes the form eq. (1), where the scalar charge is obtained from the radial flux as in eq. (24). Assuming the axion gradient is approximately localised to near the surface and the dilaton does not deviate from its surface value within the body appreciably yields

$$L \simeq \frac{R_{\text{roll}}^3}{3} V_{,\chi}(\chi_c, \mathbf{a}_-) + 2\beta M_{\text{pl}} \Phi_N(R_s) R_s + R_s^2 \left(\frac{\Delta \mathbf{a}}{\ell_a} \right)^2 W(\chi_s) W_{,\chi}(\chi_s) \ell_a, \quad (58)$$

where the second term defines the single-field charge as in eq. (15) and the final term is the axion-induced surface contribution arising purely from the two-derivative σ -model structure. The scalar charge depends on the boundary value χ_s and the central value χ_c . They are not independent variables. Indeed, this emanates from the way the solutions to the dynamical equations are obtained, i.e. by specifying the value of χ_c and imposing that $\chi' = 0$ at the origin. This implies the dependence $\chi_s(\chi_c)$. Varying χ_s therefore provides an accurate proxy for varying χ_c when selecting the equilibrium configuration.

D. Energy decomposition

The total static energy for a spherically symmetric configuration is

$$E = 4\pi \int_0^\infty dr r^2 \left[\frac{1}{2} \chi'^2 + \frac{1}{2} W^2 \mathbf{a}'^2 + V(\chi, \mathbf{a}) + A(\chi) \rho_m(r) \right] = E_{\text{in}} + E_{\text{sh}} + E_{\text{out}}, \quad (59)$$

where we have split the energy up by the regions from which it originates, the interior (E_{in}), the axion shell (E_{sh}) and the exterior (E_{out}). In the interior region the fields do not vary much and this gives

$$E_{\text{in}} = \frac{4\pi}{3} R_s^3 \left[V(\chi_c, \mathbf{a}_-) + A(\chi_c) \rho_c \right], \quad (60)$$

which is independent of χ_s .

In the shell region $\alpha R_s < r < R_s$ the axion dominates the energy budget due to its fast transition near the sur-

face. The shell energy is

$$E_{\text{sh}} = 4\pi \int_{\alpha R_s}^{R_s} dr r^2 \left[\frac{1}{2} (\chi')^2 + \frac{1}{2} W^2(\chi) (\mathbf{a}')^2 + V(\chi, \mathbf{a}) + A(\chi) \rho_c \right]. \quad (61)$$

If the axion dominates the varying energy density in the layer and $W(\chi)$ varies slowly across the shell, then to leading order

$$E_{\text{sh}}(\chi_s) \simeq 2\pi R_s^2 W^2(\chi_s) \frac{(\Delta \mathbf{a})^2}{\ell_a^2} \ell_a + E_0, \quad (62)$$

where E_0 contains the dilaton contribution independent of χ_s and dependent on the central value χ_c .

In the exterior, where $\chi' = L/r^2$, the gradient energy is

$$E_{\text{out}}^{(\nabla \chi)} = 2\pi \frac{L^2}{R_s}, \quad (63)$$

and the potential term contributes only a constant shift. The explicit χ_s -dependent part of the total energy is therefore

$$E_{\text{tot}}(\chi_s) = 2\pi R_s^2 W^2(\chi_s) \frac{(\Delta \mathbf{a})^2}{\ell_a^2} \ell_a + 2\pi \frac{L^2}{R_s}. \quad (64)$$

Deriving eq. (64) requires neglecting the explicit interior contribution eq. (60), which depends primarily on the central value χ_c . As stated previously, however, the surface and central values are tightly correlated, as illustrated in Figure 8. In principle these terms should be retained for complete precision; however, extremising the energy would then require the explicit functional forms of $V(\chi, \mathbf{a})$ and $A(\chi)$, which this derivation is agnostic about. We therefore drop these terms and verify their negligibility in the regimes of interest below.

E. Energy minimisation and suppression of the dilaton charge

The energy depends on a single variable, i.e. the central value χ_c , as the boundary value χ_s is a function of χ_c obtained by solving the dynamical equations of motion. In practice screening will impose that the terms in the axion contribution proportional to $\left(\frac{\Delta \mathbf{a}}{\ell_a} \right)^2$ are large implying that one can neglect the variation of the terms involving the interior value χ_c of the dilaton and minimise directly by varying the surface value χ_s . We now derive this surface value χ_s by minimising the total energy eq. (64). To make the minimisation algebraic, and in line with the examples used in Section V, we take the exponential form for $W(\chi)$ eq. (21) (which is also representative of any monotonic kinetic prefactor relevant for the axion ramp). Appendix A illustrates the corresponding calculation for a quadratic $W(\chi)$, showing that the

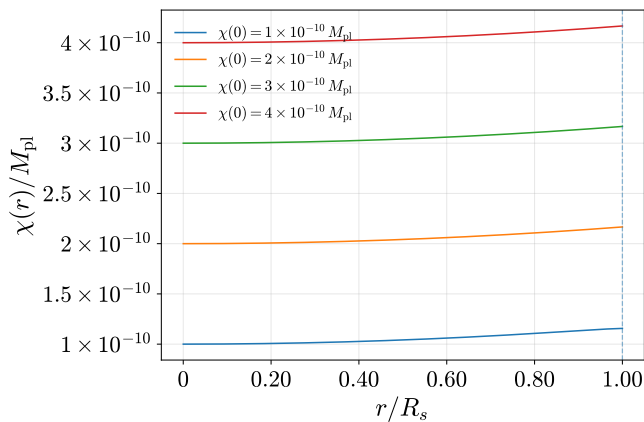


FIG. 8: Radial evolution of the dilaton field interior to an idealised constant density object (in the absence of an axion) for different central dilaton values χ_c , showing the almost exact correspondence between the surface and central values. Here we took ρ_c to correspond to the surface density of the Earth with $V_0 = 0.5\rho_c$ and $\rho_{\text{env}} = 0.1\rho_c$ and $W_0 = 1$.

structure of the result is generic. The key point is that L itself depends on χ_s through the axion-induced surface contribution to the flux balance eq. (58), which in this regime is controlled by the two-derivative interaction $W(\chi)W_{,\chi}(\chi)(\mathbf{a}')^2$.

Minimising eq. (64) with respect to χ_s yields the algebraic condition

$$\frac{R_s \ell_a}{\ell_a^2} \frac{(\Delta \mathbf{a})^2}{M_{\text{pl}}^2} W^2(\chi_s) = -\frac{1}{2\zeta^2} (4\zeta\beta \Phi_N(R_s) + 1). \quad (65)$$

Because the left-hand side is manifestly positive, eq. (65) has a solution only if

$$4\zeta\beta \Phi_N(R_s) + 1 < 0, \quad \text{i.e. } \zeta\beta < 0 \text{ and } |4\zeta\beta \Phi_N| \gtrsim 1. \quad (66)$$

Which is saying physically, $W(\chi)W_{,\chi}(\chi)$ must oppose the matter-induced pull in the flux balance so that the system can lower its total energy by reducing the exterior gradient energy L^2/R_s , and it must oppose the matter-induced pull by a large amount, hence a strong coupling between the axion and dilaton is required.

For an exponential W , eq. (65) determines the surface value of the dilaton χ_s explicitly:

$$\chi_s = \frac{M_{\text{pl}}}{2\zeta} \ln \left[-\frac{\ell_a}{R_s} \frac{M_{\text{pl}}^2}{(\Delta \mathbf{a})^2} \frac{1}{2\zeta^2} \frac{4\zeta\beta \Phi_N(R_s) + 1}{W_0^2} \right], \quad (67)$$

with the logarithm understood to be real precisely when the sign condition eq. (66) is satisfied.

The derivation of eq. (67) assumes that the dominant χ_s dependence of the total energy arises from the axion-driven surface contribution, while the implicit dependence entering through the interior value χ_c is subleading. The validity of this approximation can be tested

directly by performing a full numerical energy minimisation of the coupled system, the methodology of which is discussed in Section B. This is shown in Figure 9, where the total energy eq. (59) is evaluated numerically as a function of χ_s . The analytic prediction eq. (67) reproduces the location of the numerical minimum to within $\lesssim 10^{-11} M_{\text{pl}}$ across the range of axion ramp widths considered. We can see that the approximation is best for thinner axion gradients and becomes inaccurate as one considers more gradual axion ramps, going beyond the fast transition window approximation made in the analytic derivation. This is because the dominant energy contribution becomes no-longer localised within a small shell at the surface, as was assumed in eq. (62), and one needs to include additional corrections from contributions outside this shell width as the axion gradient widens. We have further verified that this residual offset produces no observable change in the inferred charge suppression, and the resulting L/L_0 (and hence β_{eff}) remains unchanged at the level relevant for the screening conclusions of this work.

Inserting eq. (65) into the flux expression eq. (58) (and using $W_{,\chi} = (\zeta/M_{\text{pl}})W$ for the exponential prefactor) gives

$$\frac{L}{L_0} = \frac{-\frac{M_{\text{pl}}}{2\zeta} + \frac{R_{\text{roll}}^3}{3R_s} V_{,\chi}(\chi_c, \mathbf{a}_-)}{2\beta M_{\text{pl}} \Phi_N(R_s)}, \quad (68)$$

showing explicitly how the axion-induced surface term suppresses the usual single-field contribution to the charge, up to a remainder controlled by $1/\zeta$ and by the (model-dependent) potential contribution from $V_{,\chi}$. This shows that screening can occur even when there is no parametrically thin rolling layer: what is reduced is the *amplitude* of the exterior $1/r$ tail, not necessarily the radial width over which χ varies.

Successful screening then requires an extremely large *negative* value for ζ given that $V_{,\chi}$ should independently be small for a cosmologically light dilaton, proving that screening works if $\frac{W_{,\chi}}{W} < 0$. If $\Phi_N \sim 10^{-6}$, corresponding to the Solar surface Newtonian potential, and imposing a reduction of the effective coupling by a factor of the order of 10^3 to pass solar system tests of gravity, one then requires $|\zeta| \gtrsim 10^9$ for such suppression of the exterior charge for $\beta \sim \mathcal{O}(1)$. We will return to all of the problems associated with realising this in a successful model in the next section.

This behaviour is cleanly exhibited by the numerical solutions shown in Figure 10 and Figure 11 for a constant density object. The dilaton profile evolves throughout the whole interior of the object, consistent with R_{roll} lying deep inside the surface (so $\Delta R = \mathcal{O}(R_s)$) meaning we are far away from the large environmental mass pinned dilaton regime, while the exterior charge is nevertheless strongly suppressed once the axion ramp is present. The BBQ/energy-minimisation mechanism therefore realises screening in the regime most relevant for a dark-energy like, cosmologically light dilaton, where $m_{\text{eff}} R_s \ll 1$.

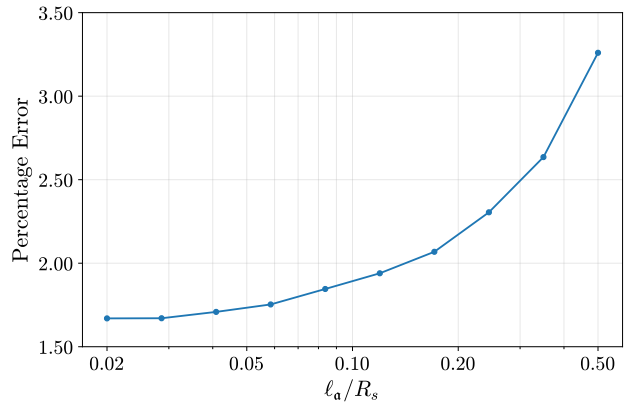
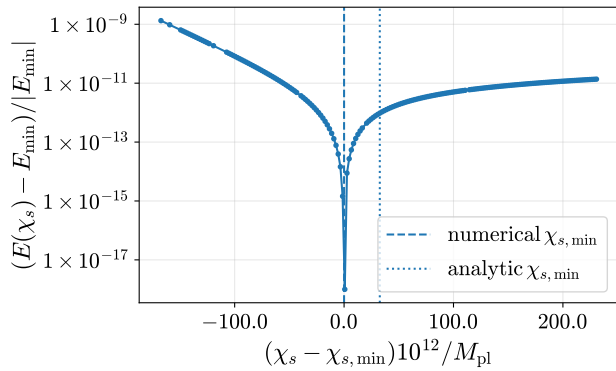


FIG. 9: **Left:** Relative difference between the Total system energy $E(\chi_s)$ and the minimum evaluated energy E_{\min} as a function of χ_s for the green curve in Figure 10, corresponding to a wide axion gradient with $\ell_a = 0.4$. We also plot the analytic prediction for the energy minimising χ_s from eq. (67) as a dotted line, compared to the numerically obtained minimum in the dashed line. **Right:** Percentage error in the analytic estimate eq. (67) compared to the numerically obtained minimum energy χ_s for different axion ramp widths.

These figures also show the efficiency of screening is preserved as one goes beyond the thin axion gradient approximation used in deriving eq. (68). Physically, the success of screening even with gradual axion gradients is a direct consequence of the large energetic cost associated with the dilaton’s exterior tail. Outside the source, $\chi' = L/r^2$, so the exterior gradient energy scales as $E_{\text{out}}^{(\nabla\chi)} \propto L^2/R_s$. The minimum–energy configuration therefore favours solutions with smaller $L \propto \chi'(R_s)$.

In the BBQ regime the system achieves this by axion backreaction. Because the axion gradient depends on the local value of $W(\chi)$, the coupled equations realise a self–regulating feedback, where shifting χ reshapes the axion contribution to the dilaton equation. For a sufficiently large hierarchy between the axion mass inside and outside the source (so that the axion adiabatically tracks its effective potential; see Section B), one finds $\alpha'(r) \propto 1/W^2(\chi)$. In the BBQ regime $W(\chi)$ is monotonic with $W_{,\chi} < 0$ over the relevant field range, so driving the dilaton to smaller χ increases $W(\chi)$. In the adiabatic regime the axion gradient is then dynamically suppressed. This prevents the axion contribution from overshooting the matter and potential terms in eq. (23). If it begins to dominate and pushes χ downwards, the resulting increase in W reduces α' , weakening the axion backreaction and stabilising the system near the value of χ_s for which the net sourcing in the rolling region is minimised. This is why the dilaton profile is ruthlessly flattened and the charge is largely suppressed in Figure 10 and Figure 11.

Figure 12 shows that the same mechanism operates for a stellar density distribution, where one might naively expect the screening efficiency to be degraded. Instead, the dilaton gradient and charge persist up to the radius at which the axion begins its transition. The efficiency of the screening therefore depends on the detailed axion dynamics, with broader axion gradients producing more

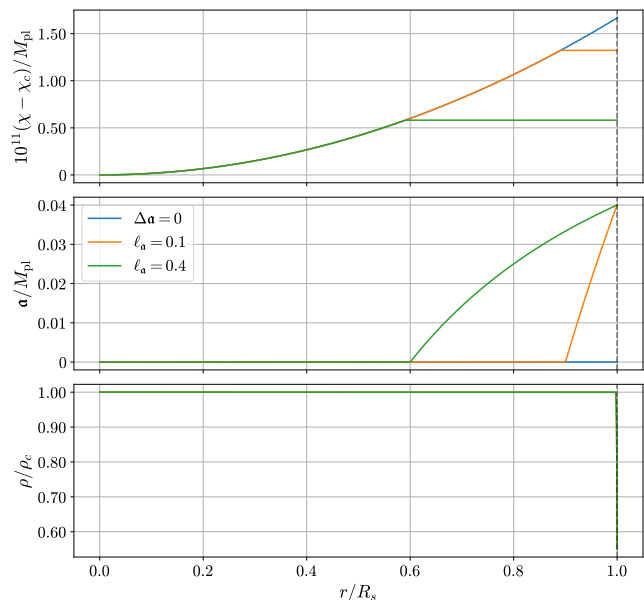


FIG. 10: Radial profiles (in units of r/R_s) illustrating the energy–minimisation (BBQ) regime, for different axion boundary jumps $\Delta\alpha = 0.04$. Here we took $W_0 = 1$, $\beta = 0.2$, $\zeta = -2 \times 10^{10}$. This is using the numerical energy minimisation scheme to determine χ_s , outlined in Section B.

comprehensive screening. These systems can therefore exhibit *enhanced* screening efficiency relative to configurations with a sharp density discontinuity at the surface. Physically, a smooth density profile allows for a more gradual axion transition throughout the stellar interior, which in turn screens the dilaton deeper inside the object.

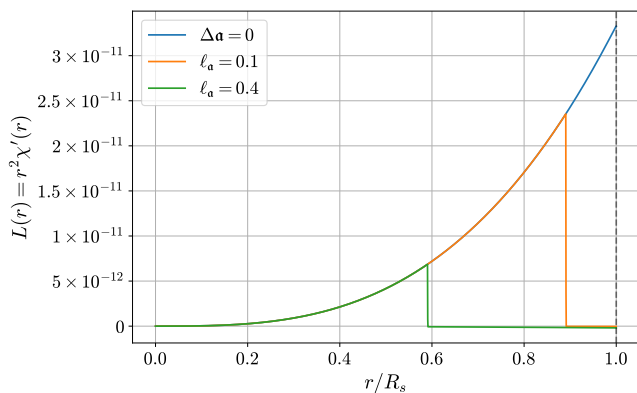


FIG. 11: Dilaton charge $L(r) \equiv r^2 \chi'(r)$ profiles for the BBQ flux solutions as a function of radius r/R_s for different axion ramp widths ℓ_a . The $\Delta a = 0$ curve reproduces the single-field baseline single field result.

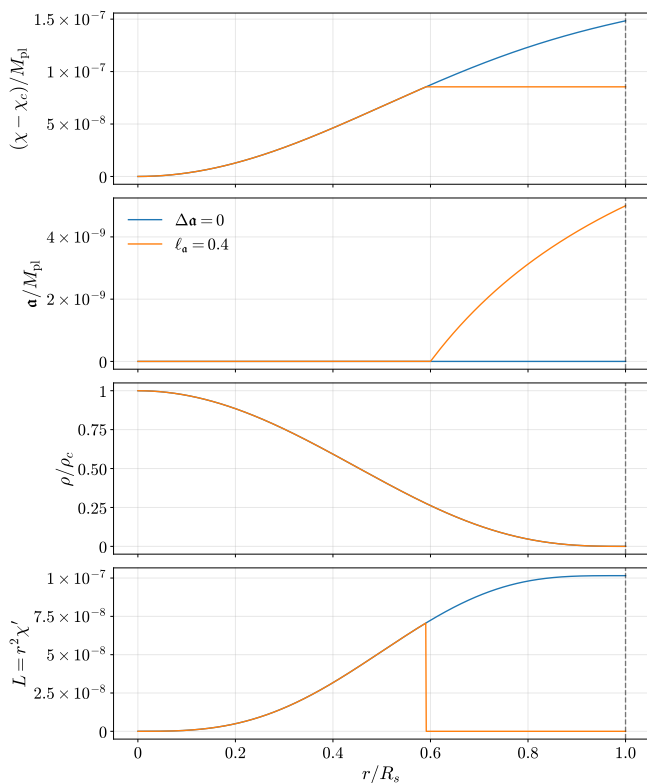


FIG. 12: Radial profiles in the presence of a stellar mass density (see Section B for details) illustrating the energy-minimisation (BBQ) regime, for an axion boundary jump $\Delta a = 4 \times 10^{-9}$. Here we took $W_0 = 1$, $\beta = 0.2$, $\zeta = -2 \times 10^{10}$. This is using the numerical energy minimisation scheme to determine χ_s , also outlined in Section B.

VII. THE DILATON REVISITED

The preceding sections show that, in multi-field systems, geometric localisation of a profile and suppression of the observable fifth force need not coincide. In the pinned, two-minima regime the axion backreaction can drive the dilaton transition into an increasingly thin near-surface layer, but the conserved exterior charge remains set by the global flux balance. As a result, a thinner rolling region is neither necessary nor sufficient for screening: it can be achieved without reducing the long-range $1/r$ tail, and can even enhance the charge once the axion-induced contribution to the flux is accounted for. Nevertheless, localisation remains phenomenologically relevant in its own right. Many laboratory and Solar-System tests probe the detailed field gradients interior to sources, such as through stellar burning and geochemical constraints, so confining large gradients to a narrow surface layer can reduce the spacetime volume over which such effects operate even when the asymptotic force is controlled by the unchanged exterior charge.

By contrast, when the dilaton is ultra-light on astrophysical scales, or when its effective potential admits no relevant density-dependent minima, the thin-shell picture ceases to be parametrically well defined. In this unpinned regime the dilaton typically rolls throughout the interior, and viable screening must proceed by suppressing the net scalar charge directly. In the axio-dilaton system this occurs through the energy-minimisation (BBQ) mechanism. In this regime the coupled configuration dynamically selects a surface value that lowers the total static energy by reducing the exterior gradient energy (by leveraging the axion-dilaton kinetic coupling, with appropriate sign and magnitude to suppress the dilaton's gradient), and hence the conserved charge, without requiring a geometrically thin rolling layer or an object-by-object tuning of unrelated contributions.

A remaining model-building question is the size of the kinetic slope required for efficient charge suppression. In the exponential ansatz eq. (21), the strongest suppression only occurs for large negative ζ , corresponding to a rapidly varying field-space metric. Consequently, the large- $|\zeta|$ regime required for efficient charge suppression should be interpreted as an *effective* two-field description. In string compactifications the function $W(\chi)$ is fixed by the moduli-space metric, so $|\zeta|$ being large is a geometric property of the field space. It requires that the axion kinetic metric $K_{aa}(\phi^I)$ vary rapidly along the light canonically normalised direction χ , i.e.

$$|\zeta| \sim \frac{1}{2} \left| \frac{d \ln K_{aa}}{d\chi} \right| \gg 1, \quad (69)$$

rather than being an arbitrary parameter. Realising this in a UV completion therefore amounts to engineering a compactification in which the axionic decay constant changes sharply as one moves in moduli space along the χ direction, for example because the light direction is an aligned/mixed combination of several moduli so that

modest motion in χ corresponds to a large fractional change in the underlying geometric modulus controlling the axion metric. Constructing explicit compactifications that realise such an effectively large- $|\zeta|$ while maintaining parametric control (without running into the usual disasters of towers of light states and α' corrections etc.) is therefore an open model-building problem.

Finally, multi-field dynamics can introduce new sources of non-universality even when the dilaton coupling $A(\chi)$ is universal. Whenever the axion sector couples (even weakly) to composition-dependent quantities (such as baryon number in order to generate the required ramp-like structures interior to objects that we have shown give screening effects), the density-dependent equilibrium data that set the axion jump, and hence the effective ramp entering the dilaton backreaction, become object dependent through \mathbf{a}_\pm . This makes the screening of light scalars inherently object- and composition-dependent, because the same microscopic parameters need not generate the same axion ramp (or even any ramp) in environments with different matter content, for example in galaxy haloes where the dominant component is not baryonic.

VIII. CONCLUSIONS

This work has shown that a constant-coupling dilaton is not generically doomed by fifth-force bounds once its axionic partner is brought into the mix. In an axio-dilaton system the kinetic coupling makes the axion gradients feed directly into the dilaton equation. That contribution enters the flux balance that fixes the conserved exterior charge $L = r^2 \chi'$, and therefore the strength of the long-range fifth force. With $W_{,\chi} < 0$ the axion backreaction can oppose the matter-induced sourcing of the dilaton and drive L down, providing a concrete route to screening in precisely the regimes where the single-field thin-shell picture fails.

What makes the mechanism work in practice is that the system is not trying to engineer a perfect surface transition of the dilaton to the asymptotic equilibrium. In the unpinned regime, relevant for a cosmologically light dilaton and for models in which the dense-matter minimum is inaccessible on stellar and planetary scales, the configuration is selected by minimising the static energy. The dominant lever in that minimisation is the exterior tail, for which outside the source one has $\chi' = L/r^2$, so the exterior gradient energy scales as $E_{\text{out}}^{(\nabla\chi)} \propto L^2/R_s$. Reducing $|L|$ is therefore an efficient way to lower the energy, and the axion provides the channel through which the system can actually do it. Because the axion gradient itself depends on $W(\chi)$, shifting the dilaton reshapes the axion contribution to the flux, which in turn reshapes the dilaton profile. The coupled equations therefore organise a feedback that naturally steers the solution towards the low-charge regime. The effect is that screening survives when the axion ramp is not infinitesimally thin and a

finite-width transition still contributes to the same flux balance and still participates in the same energy selection. Our numerical solutions show that the suppression of L persists for broad ramps and for smooth stellar density profiles, in which the axion transition can extend into the interior.

The pinned regime tells the complementary story. When the dilaton is heavy enough to track density-dependent minima, the interior-exterior mismatch already fixes a substantial flux budget. The axion can still act with the opposite sign and partially cancel the charge, but now it is cancelling something that is enforced by pinning rather than something the system is free to relax away. As a result the cancellation is typically delicate and object dependent. The choice of axion gradient amplitude and shape that suppresses the charge for one density profile need not do so for another. This is the sense in which axion gradients can dramatically reshape the near-surface profile without guaranteeing a correspondingly small fifth force.

These results point to several natural extensions. The first is genuinely multi-body configurations. In a realistic solar system or galactic environment there is no reason to expect a single ambient value to be reached independently around each object, and matching the exterior tails of multiple bodies should induce additional gradients in the regions between them. Determining how the effective charges renormalise in that setting requires solving the coupled system with the correct collective boundary conditions. Such an effort is currently underway.

A second direction concerns environmental and composition dependence. Even if the dilaton coupling $A(\chi)$ is universal, the axion sector can introduce object dependence through the mechanism that induces its own gradient to suppress the dilaton's, since these are set by the microphysics that determines how the axion feels matter. The fact that screening does not require an infinitesimal surface jump is important here and it suggests that comparatively modest axion gradients can already be relevant, so the same physics that makes screening robust can also make equivalence-principle sensitive signatures plausible, depending on which matter species source the axion and how.

Thirdly, and complementary to the previous argument, it is known that screening in astrophysical systems behaves very differently once the spherical symmetry assumption is generalised [119]. Given that the bodies most sensitive to solar system tests of gravity all roughly obey this spherical symmetry, analysing test bodies that break this assumption, either in the lab or in astrophysical systems can provide a route to detecting modifications to gravity that are otherwise screened [120–123]. Understanding how these effects would modify multi-field systems through additional non-linearities could provide detection mechanisms not available to single field tests of modified gravity.

A fourth issue is the model-building meaning of the large negative kinetic slope required for strong suppres-

sion in the exponential ansatz $W(\chi) = W_0 e^{\zeta\chi}$. In a UV completion ζ is a property of the scalar manifold rather than a freely dialled parameter, so the question becomes whether controlled compactifications can realise an effectively large negative ζ without invalidating the two-field description.

Finally, neutron stars sit in a qualitatively different corner of parameter space. Their densities and relativistic structure can pin a dilaton that is cosmologically light, while the axion dynamics may depend sensitively on the interior composition and on strong gravity. Extending the present analysis to that regime therefore requires a relativistic treatment of the coupled fields in a realistic stellar background, but it also offers the prospect of distinctive signatures and stringent tests of multi-field screening.

More generally, the motivation for studying screening in multi-field systems extends beyond the specific axio-dilaton model considered here. Many cosmological scenarios invoke additional gravitational couplings or new propagating degrees of freedom in order to obtain nontrivial late-time dynamics, including scalar-tensor and modified-gravity models capable of producing phantom-divide crossing or other dark-sector phenomenology [124–138]. Because the same interactions generically mediate long-range scalar forces or modify

gravity on small scales, compatibility with laboratory and Solar-System tests requires that their effects be suppressed in dense environments. Screening is therefore a structural ingredient of many such cosmological constructions rather than an optional addition.

We hope these considerations motivate renewed interest in the sparsely explored landscape of multi-field astrophysical modelling.

ACKNOWLEDGEMENTS

We thank Cliff Burgess, Sergio Sevillano Muñoz and Maria Mylova for helpful and illuminating discussions. This work grew out of discussions at UK Cosmo 2024 at King’s College London. AS, CvdB, and ACD thank King’s College London for its hospitality during the programme. AS also thanks the Perimeter Institute and Kavli IPMU for their hospitality, where much of this research was carried out. AS is supported by the W.D. Collins Scholarship. CvdB is supported by the Lancaster–Sheffield Consortium for Fundamental Physics under STFC grant: ST/X000621/1. ACD is partially supported by the Science and Technology Facilities Council (STFC) through the STFC consolidated grant ST/T000694/1.

-
- [1] C. van de Bruck, G. Poulot, and E. M. Teixeira, *JCAP* **07**, 019, arXiv:2211.13653 [hep-th].
 - [2] M. Archidiacono, E. Castorina, D. Redigolo, and E. Salvioni, *JCAP* **10**, 074, arXiv:2204.08484 [astro-ph.CO].
 - [3] M. Baryakhtar, O. Simon, and Z. J. Weiner, *Phys. Rev. D* **110**, 083505 (2024), arXiv:2405.10358 [astro-ph.CO].
 - [4] M. Baryakhtar, O. Simon, and Z. J. Weiner, *Phys. Rev. D* **111**, 115026 (2025), arXiv:2502.04432 [hep-ph].
 - [5] M. Costa, C. Creque-Sarbinowski, O. Simon, and Z. J. Weiner, arXiv:2510.00098 [astro-ph.CO] (2025).
 - [6] S. Castello, Z. Wang, L. Dam, C. Bonvin, and L. Pogosian, *Phys. Rev. D* **110**, 103523 (2024), arXiv:2404.09379 [astro-ph.CO].
 - [7] X. Gan, D. Liu, D. Liu, X. Luo, and B. Yu, arXiv:2504.11522 [hep-ph] (2025).
 - [8] S. Ghosh, K. K. Boddy, and T.-T. Yu, arXiv:2511.14532 [astro-ph.CO] (2025).
 - [9] N. Frusciante *et al.* (Euclid), arXiv:2512.09748 [astro-ph.CO] (2025).
 - [10] C. Zheng, W. Liu, Z. Zhan, and W. Fang, *Res. Astron. Astrophys.* **25**, 125015 (2025), arXiv:2509.13804 [astro-ph.CO].
 - [11] M. van der Westhuizen, A. Abebe, and E. Di Valentino, *Phys. Dark Univ.* **50**, 102121 (2025), arXiv:2509.04496 [gr-qc].
 - [12] S. Bhattacharya, G. Borghetto, A. Malhotra, S. Parameswaran, G. Tasinato, and I. Zavala, *JCAP* **09**, 073, arXiv:2405.17396 [astro-ph.CO].
 - [13] Y. Olguin-Trejo, S. L. Parameswaran, G. Tasinato, and I. Zavala, *JCAP* **01**, 031, arXiv:1810.08634 [hep-th].
 - [14] E. M. Teixeira, W. Giarè, N. B. Hogg, T. Montandon, A. Poudou, and V. Poulin, *Phys. Rev. D* **112**, 023515 (2025), arXiv:2504.10464 [astro-ph.CO].
 - [15] W. J. Wolf, C. García-García, T. Anton, and P. G. Ferreira, *Phys. Rev. Lett.* **135**, 081001 (2025), arXiv:2504.07679 [astro-ph.CO].
 - [16] R. Shah, P. Mukherjee, and S. Pal, *Mon. Not. Roy. Astron. Soc.* **542**, 2936 (2025), arXiv:2503.21652 [astro-ph.CO].
 - [17] Y. Tiwari, U. Upadhyay, and R. K. Jain, *Phys. Rev. D* **111**, 043530 (2025), arXiv:2412.00931 [astro-ph.CO].
 - [18] E. M. Teixeira, G. Poulot, C. van de Bruck, E. Di Valentino, and V. Poulin, *Phys. Rev. D* **113**, 023514 (2026), arXiv:2412.14139 [astro-ph.CO].
 - [19] T. Simon, T. Adi, J. L. Bernal, E. D. Kovetz, V. Poulin, and T. L. Smith, *Phys. Rev. D* **111**, 023523 (2025), arXiv:2410.21459 [astro-ph.CO].
 - [20] Y.-M. Zhang, T.-N. Li, G.-H. Du, S.-H. Zhou, L.-Y. Gao, J.-F. Zhang, and X. Zhang, arXiv:2510.12627 [astro-ph.CO] (2025).
 - [21] E. Bellini and I. Sawicki, *JCAP* **07**, 050, arXiv:1404.3713 [astro-ph.CO].
 - [22] G. Gubitosi, F. Piazza, and F. Vernizzi, *JCAP* **02**, 032, arXiv:1210.0201 [hep-th].
 - [23] N. Frusciante and L. Perenon, *Phys. Rept.* **857**, 1 (2020), arXiv:1907.03150 [astro-ph.CO].
 - [24] G. Efstathiou, *Phil. Trans. Roy. Soc. Lond. A* **383**, 20240022 (2025), arXiv:2406.12106 [astro-ph.CO].
 - [25] G. Efstathiou, *Mon. Not. Roy. Astron. Soc.* **538**, 875 (2025), arXiv:2408.07175 [astro-ph.CO].

- [26] A. Bedroya, G. Obied, C. Vafa, and D. H. Wu, arXiv:2507.03090 [astro-ph.CO] (2025).
- [27] M. Hong, K. Mukaida, and T. T. Yanagida, No-scale Brans-Dicke Gravity – ultralight scalar boson & heavy inflaton (2025), arXiv:2503.18648 [hep-ph].
- [28] J. Bagger and E. Witten, Phys. Lett. B **118**, 103 (1982).
- [29] J. P. Conlon, Fortsch. Phys. **55**, 287 (2007), arXiv:hep-th/0611039.
- [30] M. Cicoli, Fortsch. Phys. **58**, 115 (2010), arXiv:0907.0665 [hep-th].
- [31] U. H. Danielsson and T. Van Riet, Int. J. Mod. Phys. D **27**, 1830007 (2018), arXiv:1804.01120 [hep-th].
- [32] D. Andriot, M. Rajaguru, and G. Tringas, JHEP **05**, 046, arXiv:2501.17775 [hep-th].
- [33] D. Andriot, Phys. Dark Univ. **49**, 102000 (2025), arXiv:2505.10410 [hep-th].
- [34] D. J. Kapner, T. S. Cook, E. G. Adelberger, J. H. Gundlach, B. R. Heckel, C. D. Hoyle, and H. E. Swanson, Phys. Rev. Lett. **98**, 021101 (2007), arXiv:hep-ph/0611184.
- [35] B. Bertotti, L. Iess, and P. Tortora, Nature **425**, 374 (2003).
- [36] B. Jain, V. Vikram, and J. Sakstein, Astrophys. J. **779**, 39 (2013), arXiv:1204.6044 [astro-ph.CO].
- [37] P. Touboul *et al.* (MICROSCOPE), Phys. Rev. Lett. **129**, 121102 (2022), arXiv:2209.15487 [gr-qc].
- [38] H. Desmond, P. G. Ferreira, G. Lavaux, and J. Jasche, Phys. Rev. D **98**, 083010 (2018), arXiv:1807.11742 [astro-ph.CO].
- [39] A. P. Naik, E. Puchwein, A.-C. Davis, D. Sijacki, and H. Desmond, Mon. Not. Roy. Astron. Soc. **489**, 771 (2019), arXiv:1905.13330 [astro-ph.CO].
- [40] J. Scherk and J. H. Schwarz, Nucl. Phys. B **81**, 118 (1974).
- [41] C. G. Callan, Jr., E. J. Martinec, M. J. Perry, and D. Friedan, Nucl. Phys. B **262**, 593 (1985).
- [42] E. S. Fradkin and A. A. Tseytlin, Phys. Lett. B **158**, 316 (1985).
- [43] M. Gasperini and G. Veneziano, Astropart. Phys. **1**, 317 (1993), arXiv:hep-th/9211021.
- [44] C. Brans and R. H. Dicke, Phys. Rev. **124**, 925 (1961).
- [45] R. V. Wagoner, Phys. Rev. D **1**, 3209 (1970).
- [46] T. Damour and A. M. Polyakov, Nucl. Phys. B **423**, 532 (1994), arXiv:hep-th/9401069.
- [47] T. Damour, F. Piazza, and G. Veneziano, Phys. Rev. D **66**, 046007 (2002), arXiv:hep-th/0205111.
- [48] T. Damour, F. Piazza, and G. Veneziano, Phys. Rev. Lett. **89**, 081601 (2002), arXiv:gr-qc/0204094.
- [49] T. Damour and J. F. Donoghue, Phys. Rev. D **82**, 084033 (2010), arXiv:1007.2792 [gr-qc].
- [50] P. Brax, C. van de Bruck, A.-C. Davis, and D. Shaw, Phys. Rev. D **82**, 063519 (2010), arXiv:1005.3735 [astro-ph.CO].
- [51] P. Brax, C. van de Bruck, A.-C. Davis, B. Li, and D. J. Shaw, Phys. Rev. D **83**, 104026 (2011), arXiv:1102.3692 [astro-ph.CO].
- [52] P. Brax, A.-C. Davis, B. Li, and H. A. Winther, Phys. Rev. D **86**, 044015 (2012), arXiv:1203.4812 [astro-ph.CO].
- [53] P. Brax, Phys. Rev. D **112**, 083544 (2025), arXiv:2507.16723 [astro-ph.CO].
- [54] E. Di Valentino, A. Melchiorri, and O. Mena, Phys. Rev. D **96**, 043503 (2017), arXiv:1704.08342 [astro-ph.CO].
- [55] W. Giarè, Y. Zhai, S. Pan, E. Di Valentino, R. C. Nunes, and C. van de Bruck, Phys. Rev. D **110**, 063527 (2024), arXiv:2404.02110 [astro-ph.CO].
- [56] A. Smith, M. Mylova, C. van de Bruck, C. P. Burgess, and E. Di Valentino, arXiv:2512.13544 [astro-ph.CO] (2025).
- [57] N. Schöneberg and L. Vacher, JCAP **03**, 004, arXiv:2407.16845 [astro-ph.CO].
- [58] R. Catena and J. Moller, JCAP **03**, 012, arXiv:0709.1931 [hep-ph].
- [59] C. P. Burgess, D. Dineen, and F. Quevedo, JCAP **03** (03), 064, arXiv:2111.07286 [hep-th].
- [60] R. Kallosh and A. Linde, JCAP **08** (08), 037, arXiv:2203.10437 [hep-th].
- [61] S. Alexander, H. Bernardo, and M. W. Toomey, JCAP **03**, 037, arXiv:2207.13086 [astro-ph.CO].
- [62] H. Bernardo, R. Brandenberger, and J. Fröhlich, JCAP **09**, 040, arXiv:2201.04668 [hep-th].
- [63] A. Smith, M. Mylova, P. Brax, C. van de Bruck, C. P. Burgess, and A.-C. Davis, JCAP **12**, 058, arXiv:2408.10820 [hep-th].
- [64] S. Rahimy, E. M. Teixeira, and I. Zavala, arXiv:2503.01961 [hep-th] (2025).
- [65] A. Smith, P. Brax, C. van de Bruck, C. P. Burgess, and A.-C. Davis, Eur. Phys. J. C **85**, 1062 (2025), arXiv:2505.05450 [hep-th].
- [66] A. Smith, M. Mylova, P. Brax, C. van de Bruck, C. Burgess, and A.-C. Davis, Journal of Cosmology and Astroparticle Physics **2025** (07), 023.
- [67] M. W. Toomey, E. Hughes, M. M. Ivanov, and J. M. Sullivan, arXiv:2511.23463 [astro-ph.CO] (2025).
- [68] P. Brax, C. P. Burgess, and F. Quevedo, JCAP **03**, 015, arXiv:2310.02092 [hep-th].
- [69] A. Smith, <https://github.com/Adam-Smith-2001/Multi-field-astrophysical-profiles-and-Screening> (2026).
- [70] S. R. Coleman, J. Wess, and B. Zumino, Phys. Rev. **177**, 2239 (1969).
- [71] C. P. Burgess, Ann. Rev. Nucl. Part. Sci. **57**, 329 (2007), arXiv:hep-th/0701053.
- [72] C. P. Burgess, H. M. Lee, and M. Trott, JHEP **09**, 103, arXiv:0902.4465 [hep-ph].
- [73] R. Penco, arXiv:2006.16285 [hep-th] (2020).
- [74] S. Weinberg, Physica A **96**, 327 (1979).
- [75] A. Pich, arXiv:1804.05664 [hep-ph] (2018).
- [76] M. R. Douglas and S. Kachru, Rev. Mod. Phys. **79**, 733 (2007), arXiv:hep-th/0610102.
- [77] D. Baumann and L. McAllister, *Inflation and String Theory*, Cambridge Monographs on Mathematical Physics (Cambridge University Press, 2015) arXiv:1404.2601 [hep-th].
- [78] C. Gordon, D. Wands, B. A. Bassett, and R. Maartens, Phys. Rev. D **63**, 023506 (2000), arXiv:astro-ph/0009131.
- [79] S. Groot Nibbelink and B. J. W. van Tent, Class. Quant. Grav. **19**, 613 (2002), arXiv:hep-ph/0107272.
- [80] L. Senatore and M. Zaldarriaga, JHEP **04**, 024, arXiv:1009.2093 [hep-th].
- [81] A. Achucarro, J.-O. Gong, S. Hardeman, G. A. Palma, and S. P. Patil, JHEP **05**, 066, arXiv:1201.6342 [hep-th].
- [82] G. Shiu and J. Xu, Phys. Rev. D **84**, 103509 (2011), arXiv:1108.0981 [hep-th].
- [83] J. Khoury and A. Weltman, Phys. Rev. Lett. **93**, 171104 (2004), arXiv:astro-ph/0309300.

- [84] J. Khoury and A. Weltman, *Phys. Rev. D* **69**, 044026 (2004), arXiv:astro-ph/0309411.
- [85] K. Hinterbichler and J. Khoury, *Phys. Rev. Lett.* **104**, 231301 (2010), arXiv:1001.4525 [hep-th].
- [86] C. P. Burgess and F. Quevedo, *JCAP* **04** (04), 007, arXiv:2110.10352 [hep-th].
- [87] J. Polchinski, *String theory. Vol. 2: Superstring theory and beyond*, Cambridge Monographs on Mathematical Physics (Cambridge University Press, 2007).
- [88] T. W. Grimm and J. Louis, *Nucl. Phys. B* **699**, 387 (2004), arXiv:hep-th/0403067.
- [89] J. J. M. Carrasco, R. Kallosh, A. Linde, and D. Roest, *Phys. Rev. D* **92**, 041301 (2015), arXiv:1504.05557 [hep-th].
- [90] M. Cicoli, J. P. Conlon, A. Maharana, S. Parameswaran, F. Quevedo, and I. Zavala, *Phys. Rept.* **1059**, 1 (2024), arXiv:2303.04819 [hep-th].
- [91] F. Apers, J. P. Conlon, E. J. Copeland, M. Mosny, and F. Revello, *JCAP* **08**, 018, arXiv:2401.04064 [hep-th].
- [92] C. Wetterich, *Nucl. Phys. B* **302**, 668 (1988), arXiv:1711.03844 [hep-th].
- [93] C. Wetterich, *Phys. Rev. D* **81**, 103508 (2010), arXiv:1003.3809 [hep-th].
- [94] T. Henz, J. M. Pawłowski, and C. Wetterich, *Phys. Lett. B* **769**, 105 (2017), arXiv:1605.01858 [hep-th].
- [95] C. Wetterich, *Nucl. Phys. B* **964**, 115326 (2021), arXiv:2007.08805 [hep-th].
- [96] M. Gasperini, F. Piazza, and G. Veneziano, *Phys. Rev. D* **65**, 023508 (2002), arXiv:gr-qc/0108016.
- [97] E. E. Flanagan, *Class. Quant. Grav.* **21**, 3817 (2004), arXiv:gr-qc/0403063.
- [98] C. M. Will, *Living Rev. Rel.* **17**, 4 (2014), arXiv:1403.7377 [gr-qc].
- [99] M. B. Green, J. H. Schwarz, and E. Witten, *Superstring Theory Vol. 1: 25th Anniversary Edition*, Cambridge Monographs on Mathematical Physics (Cambridge University Press, 2012).
- [100] D. J. E. Marsh, *Phys. Rept.* **643**, 1 (2016), arXiv:1510.07633 [astro-ph.CO].
- [101] C. P. Burgess and F. Quevedo, arXiv:2509.11340 [hep-th] (2025).
- [102] C. Burrage and J. Sakstein, *Living Rev. Rel.* **21**, 1 (2018), arXiv:1709.09071 [astro-ph.CO].
- [103] S. Tsujikawa, T. Tamaki, and R. Tavakol, *JCAP* **05**, 020, arXiv:0901.3226 [gr-qc].
- [104] P. Brax, A.-C. Davis, and R. Jha, *Phys. Rev. D* **95**, 083514 (2017), arXiv:1702.02983 [gr-qc].
- [105] P. Yin, R. Li, C. Yin, X. Xu, X. Bian, H. Xie, C.-K. Duan, P. Huang, J.-h. He, and J. Du, *Nature Phys.* **18**, 1181 (2022), arXiv:2405.09791 [gr-qc].
- [106] C. Burrage and J. Sakstein, *JCAP* **11**, 045, arXiv:1609.01192 [astro-ph.CO].
- [107] H. Fischer, C. Käding, and M. Pitschmann, *Universe* **10**, 297 (2024), arXiv:2405.14638 [gr-qc].
- [108] H. Oyaizu, *Phys. Rev. D* **78**, 123523 (2008), arXiv:0807.2449 [astro-ph].
- [109] H. Oyaizu, M. Lima, and W. Hu, *Phys. Rev. D* **78**, 123524 (2008), arXiv:0807.2462 [astro-ph].
- [110] B. Li, W. A. Hellwing, K. Koyama, G.-B. Zhao, E. Jennings, and C. M. Baugh, *Monthly Notices of the Royal Astronomical Society* **428**, 743–755 (2012).
- [111] P. Brax, A.-C. Davis, B. Li, H. A. Winther, and G.-B. Zhao, *Journal of Cosmology and Astroparticle Physics* **2012** (10), 002–002.
- [112] H. A. Winther and P. G. Ferreira, *Phys. Rev. D* **91**, 123507 (2015), arXiv:1403.6492 [astro-ph.CO].
- [113] H. A. Winther *et al.*, *Mon. Not. Roy. Astron. Soc.* **454**, 4208 (2015), arXiv:1506.06384 [astro-ph.CO].
- [114] P. Brax, C. van de Bruck, D. F. Mota, N. J. Nunes, and H. A. Winther, *Phys. Rev. D* **82**, 083503 (2010), arXiv:1006.2796 [astro-ph.CO].
- [115] J. G. Williams, S. G. Turyshev, and D. H. Boggs, *Phys. Rev. Lett.* **93**, 261101 (2004), arXiv:gr-qc/0411113.
- [116] J. G. Williams, S. G. Turyshev, and D. Boggs, *Class. Quant. Grav.* **29**, 184004 (2012), arXiv:1203.2150 [gr-qc].
- [117] A. Fienga, J. Laskar, P. Kuchynka, H. Manche, M. Gastineau, and C. Leponcin-Lafitte, *IAU Symp.* **261**, 159 (2010), arXiv:0906.3962 [gr-qc].
- [118] A. Fienga and O. Minazzoli, *Living Rev. Rel.* **27**, 1 (2024), arXiv:2303.01821 [gr-qc].
- [119] C. Burrage, E. J. Copeland, and J. Stevenson, *Phys. Rev. D* **91**, 065030 (2015), arXiv:1412.6373 [hep-th].
- [120] C. Burrage, B. March, and A. P. Naik, *JCAP* **04**, 004, arXiv:2310.19955 [astro-ph.CO].
- [121] A. Almasi, P. Brax, D. Iannuzzi, and R. I. P. Sedmik, *Phys. Rev. D* **91**, 102002 (2015), arXiv:1505.01763 [physics.ins-det].
- [122] P. Brax, C. van de Bruck, A.-C. Davis, D. F. Mota, and D. J. Shaw, *Phys. Rev. D* **76**, 124034 (2007), arXiv:0709.2075 [hep-ph].
- [123] T. Anson and E. Babichev, *Phys. Rev. D* **102**, 044046 (2020), arXiv:2005.05990 [gr-qc].
- [124] F. Perrotta, C. Baccigalupi, and S. Matarrese, *Phys. Rev. D* **61**, 023507 (1999), arXiv:astro-ph/9906066.
- [125] B. Boisseau, G. Esposito-Farese, D. Polarski, and A. A. Starobinsky, *Phys. Rev. Lett.* **85**, 2236 (2000), arXiv:gr-qc/0001066.
- [126] A. De Felice and S. Tsujikawa, *Phys. Rev. D* **80**, 063516 (2009), arXiv:0907.1830 [hep-th].
- [127] C. de Rham, G. Gabadadze, and A. J. Tolley, *Phys. Rev. Lett.* **106**, 231101 (2011), arXiv:1011.1232 [hep-th].
- [128] R. Kimura, T. Kobayashi, and K. Yamamoto, *Phys. Rev. D* **85**, 123503 (2012), arXiv:1110.3598 [astro-ph.CO].
- [129] A. Banijamali and B. Fazlpour, *Gen. Rel. Grav.* **44**, 2051 (2012), arXiv:1206.3299 [physics.gen-ph].
- [130] C. de Rham, A. J. Tolley, and D. H. Wesley, *Phys. Rev. D* **87**, 044025 (2013), arXiv:1208.0580 [gr-qc].
- [131] H. Y. Ip, J. Sakstein, and F. Schmidt, *JCAP* **10**, 051, arXiv:1507.00568 [gr-qc].
- [132] M. Crisostomi, M. Lewandowski, and F. Vernizzi, *Phys. Rev. D* **100**, 024025 (2019), arXiv:1903.11591 [gr-qc].
- [133] J. T. Deskins, *Constraints on Massive Gravity: A Numerical Study of Galileons*, Ph.D. thesis, Case Western Reserve University (2019).
- [134] A. Iyonaga and T. Kobayashi, *Phys. Rev. D* **104**, 124020 (2021), arXiv:2109.10615 [gr-qc].
- [135] T. Kobayashi and T. Hiramatsu, *Phys. Rev. D* **109**, 064091 (2024), arXiv:2310.11041 [gr-qc].
- [136] M. Mylova and N. Afshordi, *JHEP* **04**, 144, arXiv:2312.06066 [hep-th].
- [137] S. Tsujikawa, *Phys. Rev. D* **113**, L041301 (2026), arXiv:2508.17231 [astro-ph.CO].
- [138] Z. Yao, G. Ye, and A. Silvestri, *JCAP* **10**, 078, arXiv:2508.01378 [gr-qc].
- [139] S. Chandrasekhar, *An introduction to the study of stellar structure* (Dover Publications, 1939).

[140] R. Kippenhahn, A. Weigert, and A. Weiss, *Stellar Structure and Evolution*, 2nd ed. (Springer, 2012).

Appendix A: Quadratic kinetic prefactor

To complement the exponential kinetic prefactor used in the main text, we briefly consider a quadratic growth of the axion kinetic function. This provides a simple example in which $W(\chi)$ increases only polynomially with the dilaton, and it illustrates how the efficiency and spatial localisation of the axion backreaction depend on the rate at which the field-space metric grows.

We take

$$W^2(\chi) = 1 + \frac{(\chi - \chi_*)^2}{2\Lambda_\chi^2}, \quad (\text{A1})$$

where χ_* parametrises the location of the minimum in the kinetic sector and Λ_χ controls the rate of growth.

The qualitative behaviour of the quadratic- W solutions is shown in Figure 13 and is most transparently understood in the flux-conserving formulation used in the numerical methods outlined in Section B. Assuming there is a large hierarchy of the axion masses interior and exterior to the source (as well as the axion being heavy in both environments) so that it tracks the minimum of its effective potential, in spherical symmetry the axion equation implies a conserved radial flux J , so that

$$\mathbf{a}'(r) = \frac{J}{r^2 W^2(\chi)}. \quad (\text{A2})$$

For an axion assisted transition one needs $W_{,\chi} > 0$. As the dilaton evolves to larger values outside matter and $W(\chi)$ increases, the axion gradient is therefore dynamically quenched according to $\mathbf{a}' \propto W^{-2}$, reducing the magnitude of the axion backreaction term in the dilaton equation eq. (23). The extent of the axion forcing is thus controlled by how quickly $W(\chi)$ grows along the profile.

For an exponential prefactor, $W(\chi) \propto e^{\zeta\chi/M_{\text{pl}}}$, even modest motion of χ near the surface produces a rapid increase in W , and the axion flux is quenched efficiently. The axion gradient therefore switches off over a narrow radial interval once the dilaton begins to roll, confining the external driving effect to a thin region close to $r \simeq R_s$ and limiting the integrated impact of the axion on the dilaton profile.

By contrast, for the quadratic form eq. (A1), the increase of $W(\chi)$ is only polynomial. The quenching $\mathbf{a}' \propto W^{-2}$ is correspondingly milder, so a substantial axion gradient can persist across a broader part of the surface region while χ evolves. This sustains the two-derivative driving over a larger radial interval and leads to a stronger overall response of $\chi(r)$ than in the exponential case at otherwise comparable parameters, consistent with the profiles in Figure 13. The result is the heightened efficiency of the axion in producing a thin-shell for the dilaton.

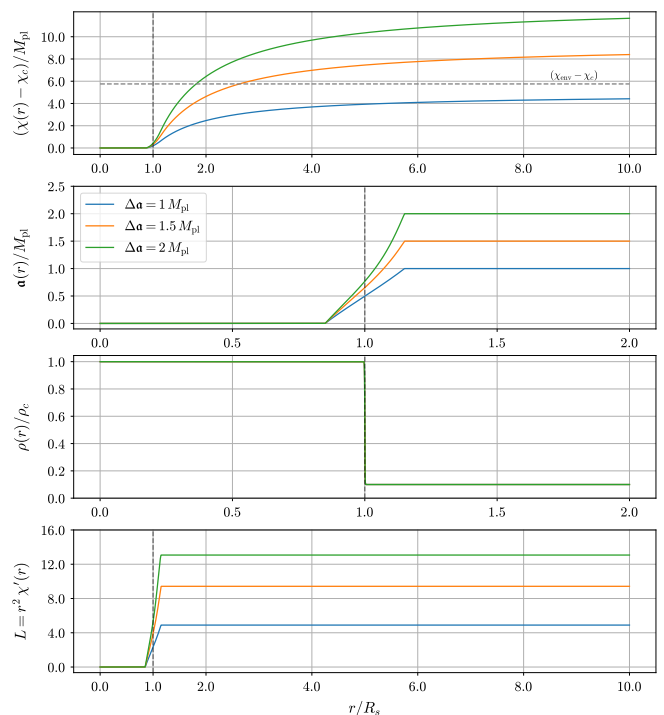


FIG. 13: Radial profiles as functions of r/R_s for a quadratic kinetic prefactor eq. (A1): dilaton $\chi(r)$ (top), axion $\mathbf{a}(r)$ (middle), and density $\rho(r)$ (bottom), for different axion boundary jumps $\Delta\mathbf{a} = \mathbf{a}_+ - \mathbf{a}_-$. We take $\Lambda_\chi = M_{\text{pl}}$ and, for numerical illustration, choose an Earth-like density $\rho_c \simeq 10^{-9} M_{\text{pl}}^2/R_s^2$, with $V_0 = 0.5 \rho_c$ and $\rho_{\text{env}} = 0.1 \rho_c$ (an unrealistically small hierarchy used only to make the effect visually clear).

BBQ Screening ($W_{,\chi} < 0$)

For completeness we record the analogue of the BBQ energy-minimisation result when the axion kinetic prefactor is quadratic rather than exponential. This illustrates the generality of the charge-suppression mechanism for monotonic kinetic sectors in which $W_{,\chi}$ does not change sign while the growth of $W(\chi)$ is parametrically milder than exponential.

Repeating the minimisation of the surface energy and exterior gradient energy in eq. (64) yields the surface value

$$\chi_s - \chi_* = \frac{2\beta \Phi_N(R_s) M_{\text{pl}}}{1 + \frac{R_s}{\ell_a} \left(\frac{\Delta\mathbf{a}}{\Lambda_\chi} \right)^2}. \quad (\text{A3})$$

So the surface value is driven to χ_* if $\frac{R_s}{\ell_a} \left(\frac{\Delta\mathbf{a}}{\Lambda_\chi} \right)^2 \gg 1$. Suggesting the axion transition amplitude $\Delta\mathbf{a}$ must be much greater than the kinetic coupling scale Λ_χ . This is in contrast to the exponential case, where the shift of the surface value is now suppressed directly by the magnitude of the axion gradient $\Delta\mathbf{a}$.

The corresponding kinetic sourcing term evaluated at

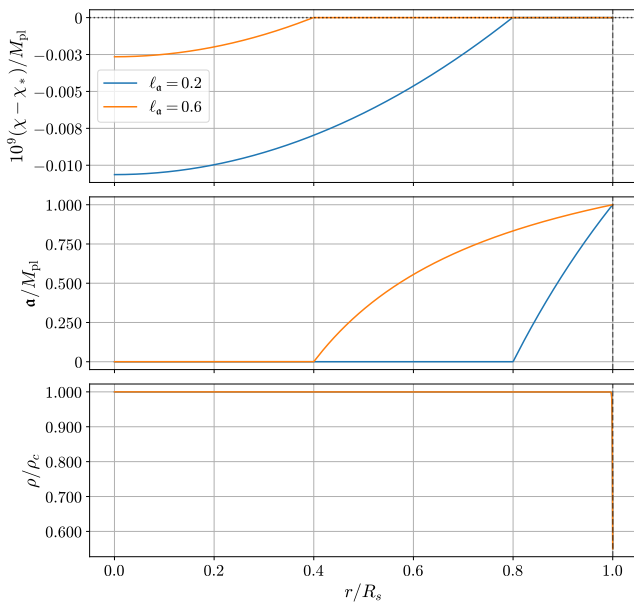


FIG. 14: Field profiles interior of a constant density object with quadratic kinetic coupling eq. (A1) between the axion and dilaton, and ρ_c corresponding to the surface density of the Earth, $V_0 = 0.5\rho_c$ and $\rho_{\text{env}} = 0.1\rho_c$. Here we used the quadratic kinetic $\Lambda_\chi = 10^{-5}M_{\text{pl}}$, $\chi_* = 10^{-9}$ and the flux conserving treatment for the axion.

the surface is

$$W(\chi_s)W_{,\chi}(\chi_s) = -\frac{2\beta\Phi_N(R_s)M_{\text{pl}}}{\Lambda_\chi^2 + R_s\ell_a\left(\frac{\Delta\alpha}{\ell_a}\right)^2}, \quad (\text{A4})$$

and the exterior scalar charge is therefore suppressed according to

$$\frac{L}{L_0} = \frac{1}{1 + \frac{R_s\ell_a}{\Lambda_\chi^2}\left(\frac{\Delta\alpha}{\ell_a}\right)^2}, \quad (\text{A5})$$

showing explicitly that, for a quadratic kinetic prefactor, increasing the axion gradient decreases the fifth force monotonically.

Taken together, eqs. (A3) and (A5) highlight a key qualitative difference between polynomial and exponential kinetic couplings. For quadratic $W(\chi)$ the charge suppression depends directly on the axion gradient and increases smoothly as $\Delta\alpha/\ell_a$ is made larger. This is confirmed in Figure 14 and Figure 15 where we can see the dilaton is very quickly driven to χ_* when the axion gradient is turned on, and held there continuously to the surfaces, suppressing the dilaton's surface charge and its effective coupling to matter.

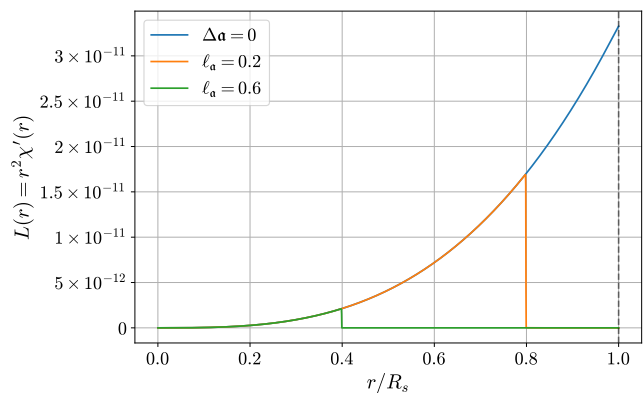


FIG. 15: Corresponding charge for the respective cases in Figure 14 using a quadratic kinetic coupling eq. (A1) between the axion and dilaton.

Appendix B: Numerical methodology

To test the analytic thin-shell estimates and to explore the fully coupled axio-dilaton system beyond the analytic approximations of Secs. III–V, we perform direct numerical integrations of the spherically symmetric field equations. The numerics retain the essential physics of the thin-shell mechanism while introducing controlled approximations that render the problem tractable on a one-dimensional radial grid. The code implementing the methods described here has been made publicly available at [69].

Overview of numerical schemes

We employ two complementary numerical strategies for the coupled axio-dilaton profiles, depending primarily on the regularity of the matter profile at the surface and the asymptotic values of the dilaton field.

For smooth stellar density profiles $\rho_m(r)$, we solve the full coupled two-field Klein-Gordon equations directly, imposing regularity at the origin and an additional appropriate boundary condition dependent on the scenario we study. This direct two-field solution is used for Figures 3 to 7.

In contrast, for an idealised near-discontinuous top-hat density transition, the coupled Klein-Gordon system becomes numerically stiff at the surface and develops spurious large gradients localised to the jump. If not compensated by a regulating asymptotic boundary condition, this can lead to runaway behaviour due to numerical instabilities. Additionally, for simulations such as BBQ energy minimisation, which are computationally intensive, solving the full two-field system becomes untractable numerically. In these cases we avoid solving the axion second-order equation across the discontinuity and instead reconstruct the axion gradient from the conserved canonical flux, treating the surface layer as a

localised source term and iterating self-consistently with the dilaton profile. This flux reconstruction scheme is the one used for Figures 2, 10 and 11 and we now outline the flux formulation details.

Axion flux reconstruction

The full radial axion equation reads

$$\frac{1}{r^2} \frac{d}{dr} (r^2 W^2(\chi) \mathbf{a}'(r)) = \mathcal{J}(r), \quad (\text{B1})$$

where $\mathcal{J}(r)$ encodes the microscopic source driving $\mathbf{a}_- \rightarrow \mathbf{a}_+$. Away from this region, the absence of external forces implies the exact conservation law

$$J \equiv r^2 W^2(\chi) \mathbf{a}'(r) = \text{constant}. \quad (\text{B2})$$

To remain agnostic about the microphysical form of $\mathcal{J}(r)$, we approximate the source region by a normalised profile $S(r)$, so that

$$\frac{1}{r^2} \frac{d}{dr} (r^2 W^2(\chi) \mathbf{a}') = J S(r). \quad (\text{B3})$$

The normalisation condition ensures that the total axion excursion is fixed to $\mathbf{a}_+ - \mathbf{a}_-$, and flux conservation is in-practice achieved by evaluating J as

$$(\mathbf{a}_+ - \mathbf{a}_-) \int dr \frac{S(r)}{r^2 W^2(\chi)} = J^{-1}. \quad (\text{B4})$$

Throughout this work we adopt a rectangular window

$$S(r) = \begin{cases} 1, & \alpha R_s < r < R_s, \\ 0, & \text{otherwise,} \end{cases} \quad (\text{B5})$$

so that the interpolation occurs in a thin layer near the surface while the interior and exterior remain frozen at \mathbf{a}_- and \mathbf{a}_+ , respectively. The dilaton-axion backreaction is treated exactly through the flux law by eq. (B2), so that wherever $W(\chi)$ grows across the shell, the axion gradient \mathbf{a}' is suppressed, stiffening the effective ramp and reproducing the behaviour dictated by the full equations of motion.

Consistency with full solutions

Figure 15 provides a direct numerical check that the flux-conservation treatment of the axion reproduces the profiles obtained from the full coupled boundary-value problem, without altering the underlying microphysical axion sector. The full reference solution (solid curves) is obtained with the stellar-profile solver described in Section B, where the axion dynamics is governed by the same microphysical potential and matter coupling as in the main text, eqs. (35) and (36).

To assess the flux formulation, we then perform an additional run in which the axion equation is replaced by a conserved flux ansatz localised to a narrow window around the surface, implemented through the window function $S(r)$ supported on $r \in (R_c - \ell_a/2, R_c + \ell_a/2)$. Crucially, the code does not change the microphysical parameters \mathbf{a}_\pm appearing in eqs. (35) and (36). In particular, \mathbf{a}_- is left untouched, so the same $U(\mathbf{a})$ is used in both the full and flux runs. Instead, the flux normalisation J is fixed *solely* by matching the endpoint values of the *full* axion solution,

$$\mathbf{a}_{\text{flux}}(r_{\text{min}}) = \mathbf{a}_{\text{full}}(r_{\text{min}}), \quad \mathbf{a}_{\text{flux}}(r_{\text{max}}) = \mathbf{a}_{\text{full}}(r_{\text{max}}). \quad (\text{B6})$$

Operationally, this determines J from the integral constraint implied by the windowed flux, while leaving \mathbf{a}_\pm (and hence eqs. (35) and (36)) unchanged.

With this setup, any difference between the solid (full) and dashed (flux) curves in Fig. 16 is attributable to the flux ansatz itself rather than to retuning the axion microphysics. The close agreement observed therefore validates the flux-conservation approximation as a faithful representation of the full coupled solution in the regime considered.

Matter density profile

Here we give the explicit functional forms of the density distributions used in the numerics throughout the paper.

Idealised planetary mass distribution

The source is modelled as a sphere of radius R_s with central density ρ_c embedded in an environment of density ρ_{env} . The central density is taken illustratively as that of the Earth's so that $\Phi_N(R_s) \sim 10^{-9}$. To avoid an unphysical discontinuity in the force at the surface we introduce a smooth transition

$$\rho_m(r) = \frac{1}{2} \rho_c \left[1 - \tanh\left(\frac{r - R_s}{\ell_\rho}\right) \right] + \frac{1}{2} \rho_{\text{env}} \left[1 + \tanh\left(\frac{r - R_s}{\ell_\rho}\right) \right], \quad (\text{B7})$$

with $\ell_\rho \ll R_s$ being the characteristic width of the surface density gradient. This retains the essential density contrast while remaining differentiable.

Stellar mass density distribution

For stellar applications we adopt a smoothed truncated polytropic profile (used as a simple analytic proxy

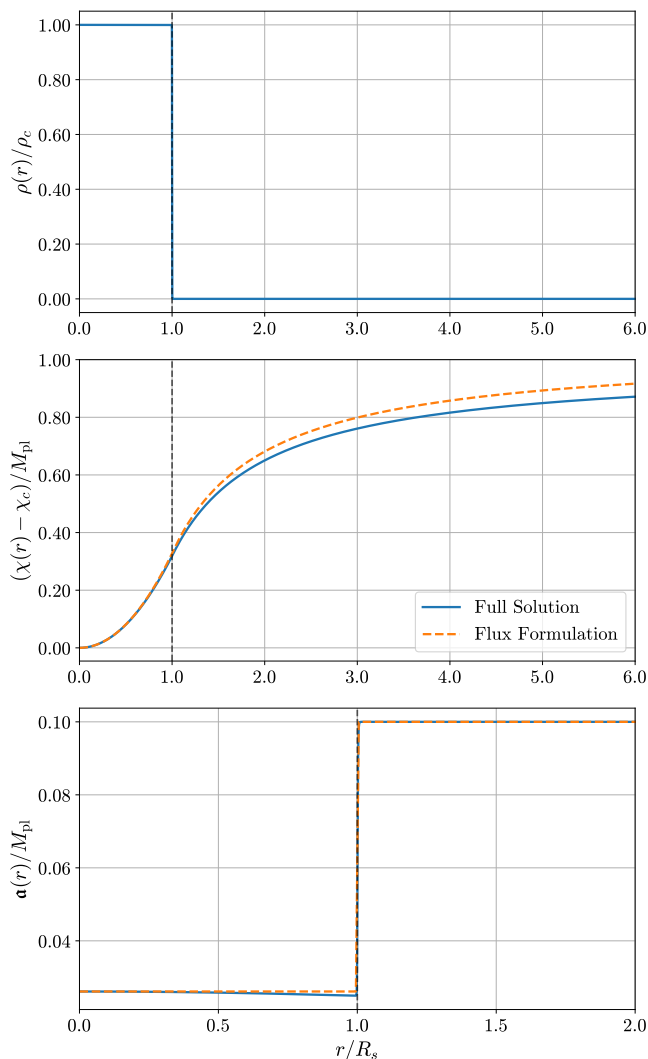


FIG. 16: Radial profiles for the coupled axion–dilaton system in a smoothed top-hat halo. **Top:** density contrast $\rho(r)/\rho_c$. **Middle:** dilaton displacement $(\chi(r) - \chi_c)/M_{\text{pl}}$ for the full coupled solution (solid) and the flux-conservation axion formulation (dashed), with the flux boundary values matched to the full solution endpoints. **Bottom:** axion field $\mathbf{a}(r)/M_{\text{pl}}$ for the same two runs.

for a Lane–Emden solution)[139, 140]. The density profile of a star falls approximately as

$$\rho_{\text{poly}}(r) = \rho_c \left[1 - \left(\frac{r}{R_s} \right)^2 \right]^{n_{\text{poly}}}, \quad r \leq R_s, \quad (\text{B8})$$

while outside we add an additional environmental density ρ_{env} for $r > R_s$. The exponent n_{poly} controls the steepness of the stellar stratification (with $n_{\text{poly}} = 3$ used as a representative choice in our numerics). The core density is taken to ensure that the surface Newtonian potential is given by $\Phi_N(R_s) \sim 10^{-6}$, which is that of the Sun.

Multi-field solver formulations

Given the different case studies considered in this paper and the differing appropriate numerical schemes for each one, we outline here the three types of solvers that were made use of for the numerical simulations of this paper, along with the corresponding plots that were produced with each.

IVP formulation in the runaway case

For sharply localised surface features (in particular the near–top–hat profiles used in eq. (B7)), the coupled system can become numerically stiff in the vicinity of $r \simeq R_s$ and can easily enter into non-physical runaway regimes. In these runs the dilaton does not reliably relax to a well-defined exterior minimum within the numerical domain, so there is no stable asymptotic condition that would select a unique boundary solution for χ . We therefore evolve the dilaton equation as an initial–value problem (IVP), imposing regularity at a small inner radius $r_{\text{in}} \ll R_s$,

$$\chi'(0) = 0, \quad \chi(0) = \chi_c, \quad (\text{B9})$$

and integrating outward to $r_{\text{out}} \gg R_s$ with a Runge–Kutta solver. When a local minimum of V_{eff} exists at the core density, we take χ_c to be that minimum.

The axion is not evolved as a second–order IVP in this regime. Instead, we fix the net excursion $\Delta \mathbf{a} = \mathbf{a}_+ - \mathbf{a}_-$ and reconstruct $\mathbf{a}'(r)$ from the conserved flux relation eq. (B2) together with the chosen source window $S(r)$, as described in eq. (B5). Since the reconstructed $\mathbf{a}'(r)$ depends on $\chi(r)$ through $W(\chi)$, while the dilaton equation depends on $\mathbf{a}'(r)$ through the backreaction term, the profiles are obtained by a Picard iteration: given a current axion profile (equivalently a current J), we integrate the dilaton IVP to obtain $\chi(r)$, update J using the normalisation condition eq. (B4), reconstruct $\mathbf{a}'(r)$, and repeat until both J and $\chi(r)$ change by less than fixed tolerances.

This is the integration scheme used for figure Figure 2.

Hybrid Axion–BVP, Dilaton–IVP solver

The pure IVP approach above is tailored to near-discontinuous surface features, for which no reliable asymptotic selection is available within a finite numerical domain. For the smooth stellar profiles considered in eq. (B8), the exterior evolution is well behaved and the physically relevant branch of the axion field is most cleanly imposed by boundary conditions at large radius. In this regime we therefore adopt a hybrid scheme. We evolve the dilaton as an IVP from the regular interior, while solving the axion as a boundary-value problem (BVP) to enforce the desired asymptotic behaviour. The two fields are coupled by a Picard iteration.

At a given iteration, we first hold $\chi(r)$ fixed and solve the full second-order axion equation as a boundary-value problem, supplying the χ -dependence of the coefficients through interpolation of the current dilaton iterate (including χ' where required). We impose regularity at the origin and fix the exterior branch by the asymptotic value

$$\mathbf{a}'(0) = 0, \quad \mathbf{a}(r_{\max}) = \mathbf{a}_+, \quad (\text{B10})$$

with $r_{\max} \gg R_s$ chosen large enough that the solution has reached its asymptotic regime. With the updated axion profile held fixed, we then integrate the dilaton equation outward as an IVP with interior initial conditions

$$\chi(0) = \chi_c, \quad \chi'(0) = 0, \quad (\text{B11})$$

where χ_c is determined from the local minimum condition of V_{eff} at the core density. To resolve the surface region efficiently, the IVP is evolved with a reduced maximum step size in a band around $r \simeq R_s$.

Starting from smooth initial guesses for (χ, \mathbf{a}) , we alternate the axion-BVP update and the dilaton-IVP update until both profiles stabilise. The axion update is applied in Gauss-Seidel fashion so that the axion boundary conditions are satisfied at every iteration. The dilaton update is damped,

$$\chi^{(n+1)} = \chi^{(n)} + \omega_\chi [\chi_{\text{IVP}}^{(n)} - \chi^{(n)}], \quad (\text{B12})$$

with ω_χ chosen to control large changes and improve stability. Convergence is declared when the maximum changes with iterations in both χ and \mathbf{a} fall below fixed tolerances.

For large excursions $\Delta \mathbf{a}$ the coupled iteration can become sensitive to the initial guess. In that case we employ a homotopy in the outer boundary value by solving a sequence of problems with \mathbf{a}_+ increased in steps, warm-starting each run from the converged solution at the previous \mathbf{a}_+ (both for the axion BVP and for the interpolated χ, χ' entering its coefficients). This is the scheme used for Figures 3 and 5. The environmental profiles in Figures 6 and 7 are obtained by wrapping the same procedure inside a bounded scan over ζ , holding all other parameters fixed.

Boundary-value formulation when V_{eff} has minima

If $V_{\text{eff}}(\chi)$ admits a density-dependent asymptotic minimum outside the matter distribution, the dilaton profile can be obtained by solving the second-order radial equation with two boundary conditions as a BVP. Regularity at the origin always enforces

$$\chi'(0) = 0. \quad (\text{B13})$$

The second boundary condition is obtained by imposing the asymptotic condition

$$\chi(r_{\max}) = \chi_{\text{env}}, \quad (\text{B14})$$

at a large radius $r_{\max} \gg R_s$, where χ_{env} is the exterior minimum of V_{eff} , and integrate inward or outward accordingly.

In this regime the axion can likewise be solved as a BVP by taking $\mathbf{a}'(0) = 0$, ensuring regularity at the origin, while the asymptotic boundary condition $\mathbf{a}(r_{\max}) = \mathbf{a}_+$ to select the correct physical transition. This procedure yields a unique pair (χ, \mathbf{a}) that satisfies the full two-field equations, and integration methods converge reliably. This is used in the modelling for Figure 4.

1. BBQ Screening

For the unpinned BBQ configurations of Figures 10 to 12 we do not solve the axion as a second-order BVP. Instead, we adopt the flux-reconstruction setup introduced above. This choice is because selecting the physical configuration requires an outer minimisation over the surface value χ_s , which entails rerunning the solver many times. Solving the full coupled two-field problem at each objective evaluation is substantially more expensive, whereas the single-field dilaton BVP with a conserved-flux treatment of the axion captures the relevant backreaction at greatly reduced cost. For the scope of this work we therefore use this reduced description in the BBQ parameter scans.

For a given trial surface value $\chi_s \equiv \chi(R_s)$ we solve the dilaton profile inside the object as a boundary-value problem on $[r_{\min}, R_s]$, enforcing regularity by imposing

$$\chi'(0) = 0, \quad \chi(R_s) = \chi_s. \quad (\text{B15})$$

The axion gradient is reconstructed from the conserved flux using eq. (B2) together with the window eq. (B5), with the flux J determined self-consistently by the normalisation condition eq. (B4). Since J depends on χ through eq. (B4) while χ depends on J through the backreaction, the coupled solution at fixed χ_s is obtained by the same damped fixed-point iteration described in the preceding subsection.

The physical configuration is then selected by minimising the total energy as a function of the surface value χ_s . For each χ_s we evaluate

$$E_{\text{full}}(\chi_s) = 4\pi \int_0^{R_s} dr r^2 \left[\frac{1}{2}(\chi')^2 + \frac{1}{2}W^2(\chi)(\mathbf{a}')^2 + V(\chi) + A(\chi)\rho(r) \right] + \frac{2\pi}{R_s} L^2, \quad (\text{B16})$$

where the last term accounts for the exterior tail with constant L . We locate the minimum by a coarse scan in χ_s over a fixed bracket followed by bounded local refinements around the best scan candidates, and record the full set of objective evaluations for diagnostic plots of $E_{\text{full}}(\chi_s)$.